

AN ABSTRACT OF THE THESIS OF

ROBERT JAMES BARDAY for the MASTER OF SCIENCE  
(Name) (Degree)

in Oceanography presented on December 19, 1973  
(Major) (Date)

Title: STRUCTURE OF THE PANAMA BASIN FROM MARINE  
GRAVITY DATA

Abstract approved: \_\_\_\_\_

Redacted for privacy

Richard W. Couch

In order to quantitatively examine the crustal structure of the Panama Basin without the benefit of local seismic refraction data, the following assumptions were made: (1) No significant lateral changes in density take place below a depth of 50 km. (2) The densities of the crustal layers are those of a 50-km standard section derived by averaging the results of 11 seismic refraction stations located in normal oceanic crust 10 to 40 million years (m. y.) in age. (3) The density of the upper mantle is constant to a depth of 50 km. (4) The thickness of the oceanic layer is normal in that region of the basin undergoing active spreading, exclusive of aseismic ridges. (5) The thickness of the transition layer is 1.1 km everywhere in the basin. Subject to these assumptions, the following conclusions are drawn from the available gravity, bathymetry, and sediment-thickness data: (1) Structurally, the aseismic ridges are surprisingly similar, characterized by a blocky, horst-like profile, an average depth of less than

2 km, an average depth to the Mohorovicic discontinuity of 17 km, and an average free-air anomaly of greater than +20 mgal. The fact that their associated free-air anomalies increase from near zero at their seaward ends to greater than +40 mgal at their landward ends suggests that the Cocos and Carnegie ridges are uplifted at their landward ends by lithospheric bending. (2) The centers of sea-floor spreading and fracture zones are characterized by a shoaling of the bottom and an apparent deepening of the Mohorovicic discontinuity. The only exception to this generalization is the northern end of the Panama fracture zone between the Cocos and Coiba ridges. (3) The Panama fracture zone and the fracture zone at  $85^{\circ}20'W$  longitude divide the Panama Basin into three provinces of different crustal thickness. Between these two fracture zones the crustal thickness is normal; west of  $85^{\circ}20'W$  longitude it is greater than normal; and east of the Panama fracture zone it is less than normal. (4) In that part of the Panama Basin east of the Panama fracture zone there is a major discontinuity at  $3^{\circ}N$  latitude between a smooth, isostatically compensated crust to the south and an extremely rugged, uplifted crust to the north. An explanation for this discontinuity is the effect of the inflection in the shape of the continental margin at  $3^{\circ}N$  latitude on the eastward subduction of the Nazca plate.

Structure of the Panama Basin  
From Marine Gravity Data

by

Robert James Barday

A THESIS

submitted to

Oregon State University

in partial fulfillment of  
the requirements for the  
degree of

Master of Science

June 1974

APPROVED:

Redacted for privacy

---

Associate Professor of Geophysics  
in charge of major

Redacted for privacy

---

Dean of School of Oceanography

Redacted for privacy

---

Dean of Graduate School

Date thesis is presented December 19, 1973

Typed by Susie Kozlik for Robert James Barday

## ACKNOWLEDGEMENTS

This research was conducted under the supervision of Dr. Richard W. Couch. I am grateful for his time, advice, and much needed encouragement, especially during the preliminary stages of data analysis and thesis preparation.

I am also grateful to Michael Gemperle and Ken Keeling for their help and suggestions during the processing of the data used in this research.

All of the figures presented herein were drafted by Janet Gemperle. I am especially grateful for her patience and skill in correcting several of my mistakes.

A note of appreciation is extended to Dr. Richard J. Blakely for his prompt review of this thesis on very short notice.

My wife, Judy, and daughter, Cynthia, deserve special mention for their patience and understanding during the many evenings and weekends I spent working on this research.

During my tenure as a graduate student, I was the recipient of a most appreciated Texaco Inc. Fellowship.

This research was supported by the Office of Naval Research, contract N00014-67-A-0369-0007 under project NR 083-102. .

# TABLE OF CONTENTS

	<u>Page</u>
INTRODUCTION	1
PREVIOUS WORK	3
Physiography, Structure, and Tectonics	3
Sea-Floor Spreading	6
Tectonic History	8
Gravity	9
FILTERED BATHYMETRY AND FREE-AIR GRAVITY ANOMALY MAPS	10
Quantity and Distribution of Data Relative to Complexity of Structure and Bathymetry	10
Filtering of Surface-Ship Data	12
Phase 1 -- Gridding and Averaging	12
Phase 2 -- Further Averaging and Coordinate Assignment	14
Example	16
Maps Construction	18
Discussion of Maps	18
Filtered Bathymetry Map	18
Filtered Free-Air Gravity Anomaly Map	22
ASSUMPTIONS MADE IN THE CONSTRUCTION OF CRUSTAL MODELS	27
No Significant Lateral Changes in Density Take Place Below a Depth of 50 KM	27
The Densities of the Crustal Layers Are Equal to Those of the Standard Section	29
The Density of the Upper Mantle is Constant to a Depth of 50 KM	30
The Thickness of the Oceanic Layer is Normal in Regions Undergoing Active Spreading, Exclusive of Aseismic Ridges	32
The Thickness of the Transition Layer is 1.1 KM	34
CRUSTAL SECTIONS	37
Determination of Mantle Density and Construction of Crustal Sections	37
Crustal and Subcrustal Cross Sections	40
Profile AA'	42
Profile BB'	45
Profile CC'	48

	<u>Page</u>
MOHOROVICIC DISCONTINUITY MAP	51
Computation of Depth to the Mohorovicic Discontinuity and Construction of Map	51
Discussion of Map	52
SYNTHESIS AND CONCLUSIONS	56
BIBLIOGRAPHY	68
APPENDICES	
Appendix 1. Data Flow and Computer Program Docu- mentation	74
Appendix 2. General Discussion and Derivation of a 50-km Standard Section	88

## LIST OF FIGURES

<u>Figure</u>	<u>Page</u>
1     Physiographic and tectonic map showing the location of profiles	4
2     Location map of surface-ship gravity meter tracklines and submarine pendulum stations	11
3     Diagram illustrating Phase 2 in the filtering of surface-ship data	15
4     Example of the method used to filter bathymetry and free-air gravity anomalies	17
5     Map of filtered bathymetry	19
6     Map of filtered free-air gravity anomalies	23
7     Diagram and equations for infinite-slab model	28
8     Diagram illustrating the distribution of densities for the sediment, transition, oceanic, and mantle layers	31
9     Thickness of the oceanic layer with age	33
10    Diagram illustrating the argument for a constant 1.1-km thickness for the transition layer	35
11    Crustal and subcrustal cross section for free-air gravity anomaly Profile AA'	43
12    Crustal and subcrustal cross section for free-air gravity anomaly Profile BB'	46
13    Crustal and subcrustal cross section for free-air gravity anomaly Profile CC'	49
14    Map of the computed depth to the Mohorovicic discontinuity	53
15    Alternative crustal sections for the Carnegie Ridge	57



## LIST OF APPENDIX FIGURES

<u>Figure</u>		<u>Page</u>
16	Diagram illustrating the flow of data	75
17	Location map for seismic refraction stations used for standard section determination	95
18	Distribution of the gravitational attraction of the 50-km sections determined for each of the seismic refraction stations	98

## LIST OF TABLES

<u>Table</u>		<u>Page</u>
1	Computed oceanic layer thickness in region of normal oceanic crust and subcrust	39
2	Standard section comparison	89
3	Computation of 50-km standard section	97

# STRUCTURE OF THE PANAMA BASIN FROM MARINE GRAVITY DATA

## INTRODUCTION

The Panama Basin is the region of the Eastern Equatorial Pacific that is bounded on the north and east by Central and South America and on the south and west by the Carnegie and Cocos ridges. It is an extremely complex region, encompassing portions of the Cocos and Nazca lithospheric plates and containing an active center of sea-floor spreading, several major fracture zones, a marginal trough sequence, the terminal ends of the Peru-Chile and Middle America trenches, a large graben, two major aseismic ridges, and several smaller passive and abnormally shallow structures.

In 1969, this region was the site of two geophysical surveys. The R/V Yaquina of Oregon State University (van Andel et al., 1971a) conducted a survey of the entire Panama Basin in an effort to resolve its regional tectonics. The National Oceanic and Atmospheric Administration Ship Oceanographer (Grim, 1970a) made a detailed survey of the Panama fracture zone, the easternmost fracture zone in the basin, in order to study its postulated connection (Molnar and Sykes, 1969) with the Galapagos rift zone, the active center of sea-floor spreading between the Cocos and Nazca lithospheric plates.

These surveys, both controlled by satellite navigation, produced a large quantity of surface-ship gravity measurements, having an expected accuracy of better than  $\pm 5$  mgal (Couch, 1969; Barday,

1971). The purpose of this study is to learn as much as possible from these data about the geologic structure of the Panama Basin.

## PREVIOUS WORK

### Physiography, Structure, and Tectonics

Figure 1 shows the major physiographic and tectonic features of the Panama Basin. The detailed discussion of these features by van Andel et al. (1971a) is summarized below.

Forming the western and southern boundaries of the basin, the Cocos and Carnegie ridges are aseismic features that line up with but do not meet at the Galapagos pedestal; the Cocos ridge is separated from this feature by a broad, low zone 2000 m to 2600 m deep. These ridges, strikingly similar in relief and sediment cover, are also similar to the Coiba and Malpelo ridges. At its northern end, the Cocos ridge joins the continental margin and appears to completely separate the Middle America trench and the Panama Basin. Similarly, the Peru-Chile trench shoals abruptly and loses its identity in the gap between the continental margin and the eastern end of the Carnegie ridge.

At a longitude of approximately  $82.5^{\circ}\text{W}$ , the north-south-trending Panama fracture zone (Molnar and Sykes, 1969) divides the basin into two geologically distinct regions, hereafter referred to as the western and eastern basins.

The area to the west of the Panama fracture zone is occupied by a broad basin that deepens from 2200 m in the west to 3400 m in the

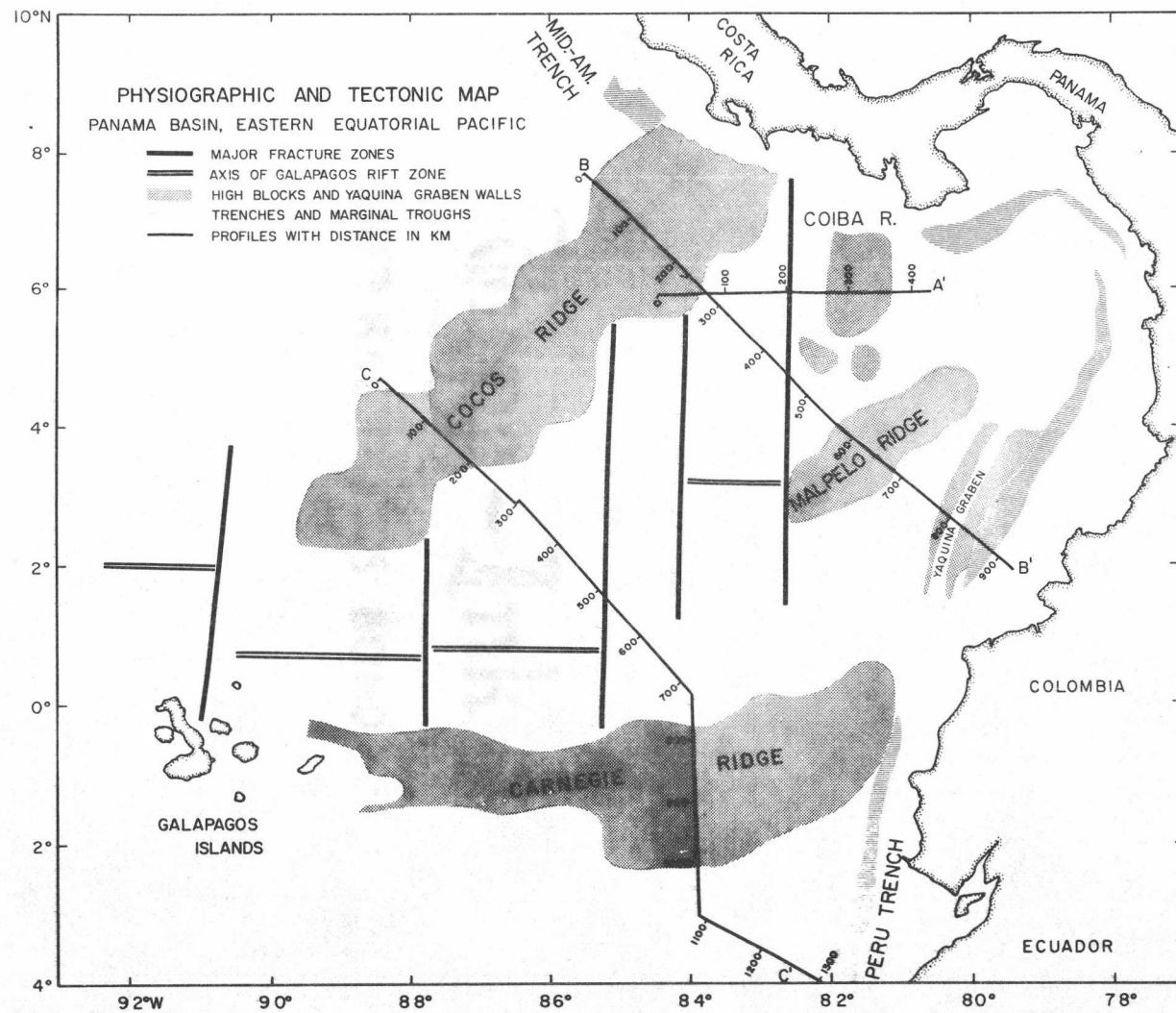


Figure 1. Physiographic and tectonic map showing the location of profiles. (Modified from van Andel *et al.*, 1971a).

east. As indicated by magnetic anomalies (Grim, 1970b), earthquake epicenters (Molnar and Sykes, 1969), and bathymetry (Sclater et al., 1971), this area is undergoing sea-floor spreading at the crest of the Galapagos rift zone. Located approximately midway between the two aseismic ridges, the Galapagos rift zone is offset by several smaller fracture zones. Although faulting along these fracture zones appears to cause left-lateral offsets in the south flank of the Cocos ridge, contrary to the right-lateral motions indicated by earthquake studies, there are no offsets in the northern boundary of the Carnegie ridge and no evidence that the fracture zones extend into this ridge for any distance.

The area east of the Panama fracture zone is highly complex. It contains several abnormally shallow structures, a marginal trough sequence, and a large, well-defined graben. Located in an undulating terrain, with a regional depth ranging from 3000 m to 3600 m, the abnormally shallow structures are similar in relief and sediment cover to the Cocos and Carnegie ridges, but much smaller. Marginal troughs parallel the continental margin from the northeastern end of the Carnegie ridge to the eastern edge of the Coiba ridge. The Yaquina graben is one of the most striking features of the eastern basin. Between  $2^{\circ}\text{N}$  and  $4^{\circ}\text{N}$  latitude, the graben consists of a deep, steep-sided trough, with a level floor bordered by faults. It begins at the

gap between the Carnegie ridge and the continental margin and extends northward away from the margin to  $5^{\circ}\text{N}$  latitude where its identity is lost in complex terrain. Along its length, it is offset several times by right-lateral faults of a northeast-trending fault system.

### Sea-Floor Spreading

No magnetic anomalies in the eastern basin have been correlated with the geomagnetic time scale (cf. Heirtzler et al., 1968). Therefore, in terms of sea-floor spreading, this region of the Panama Basin is an enigma.

Sea-floor spreading, however, is well documented in the western basin by large-amplitude magnetic anomalies, which result from east-west lineations near the magnetic equator. From the triple junction, at  $2^{\circ}11'\text{N}$  latitude,  $102^{\circ}10'\text{W}$  longitude (Hey et al., 1972), of the Pacific, Cocos, and Nazca lithospheric plates, the Cocos-Nazca spreading center, or the Galapagos rift zone, extends into the basin through the gap between the Galapagos pedestal and the Cocos ridge. From there on, it approximately bisects the western basin and terminates against the Panama fracture zone.

The reported spreading rate across this rift zone is variable, partially because of its proximity to the pole of sea-floor spreading at  $2^{\circ}\text{N}$  latitude,  $131^{\circ}\text{W}$  longitude (Hey et al., 1972) and partially



because of the scatter in the data. Because van Andel et al. (1971a) and Grim (1970a) reported rates of 2.8 cm/yr and 3.1 cm/yr, respectively, for the segment of the Galapagos rift zone just west of the Panama fracture zone, 3.0 cm/yr was the spreading rate chosen for the calculations in this research. However, the more recent works of Herron (1972), Sclater and Klitgord (1973), and Minster et al. (In press) indicate that a better figure, at least for the present spreading rate, is 3.3 cm/yr.

Anomaly 5 (Pitman et al., 1968) (10 m.y. B. P.) is the oldest magnetic anomaly found in the western basin. According to Herron (1972), this anomaly is found both north and south of the easternmost section of the Galapagos rift zone, named the Costa Rica rift zone by Grim (1970b). Furthermore, van Andel et al. (1971a) presented evidence that the age of the crust at the foot of the Cocos ridge decreases to the west. The most problematic feature in the observed magnetic anomaly pattern, however, is an asymmetry in the anomalies associated with the central portion of the Galapagos rift zone between  $85.5^{\circ}\text{W}$  and  $88^{\circ}\text{W}$  longitude. Sclater and Klitgord (1973) observed symmetrical spreading to anomaly 2' (0-3 m.y. B. P.). To the south, the identifiable anomalies terminate against the foot of the Carnegie ridge. To the north, the amplitude decreases by a factor of two, and anomalies 3 through the beginning of 5 (4-9 m.y. B. P.) can be

identified, indicating that a short section of crust between anomalies 2' and 3 (3-4 m. y. B. P.) is missing.

### Tectonic History

van Andel et al. (1971a) hypothesized that the formation of the Panama Basin started with an ancestral Carnegie ridge being split lengthwise by sea-floor spreading. All present abnormally shallow structures in the basin are remnants of this ridge. As a consequence of the present position of the Cocos and Carnegie ridges relative to the spreading pole and the fact that the age of the crust abutting against the Cocos ridge appears to decrease toward the west, they believed that spreading started in the eastern part of the basin and proceeded westward in steps. Although this theory seems to account best for the similarity in sediment cover, relief, and apparent age of the abnormally shallow structures, it has some problems: the main one being the apparent asymmetry in the spreading of the Galapagos rift zone.

Another theory for the origin of the Panama Basin, advanced by Herron and Heirtzler (1967), and Raff (1968), explains the observed magnetic anomaly pattern by a change in the direction of sea-floor spreading on the East Pacific rise. This change caused secondary spreading to occur on the Galapagos rift zone. According to Holden and Dietz (1972), and Johnson and Lowrie (1972), the Cocos

and Carnegie ridges are formed by the trajectory of the Cocos and Nazca lithospheric plates over the Galapagos hot spot. The main problem with this hypothesis has been its failure to explain the origin of the eastern basin and its prediction that the maximum age of the crust in the Paname Basin is 30 m. y. (Hey et al., 1972) or 40 m. y. (Holden and Dietz, 1972). This prediction is in conflict with the regional tectonics (Herron, 1972) and the observed magnetic anomalies, both of which suggest that spreading initiated in the western basin approximately 10 m. y. B. P. However, this hypothesis is strongly supported by models of Minster et al. (In press) showing that the configuration of the Cocos and Carnegie ridges is consistent with world-wide absolute plate motions.

### Gravity

Pendulum gravity measurements made in the Panama Basin are catalogued by Heiskanen (1938), Bruins et al. (1960), and Worzel (1965). According to Worzel (1965), these data indicate that the Panama Basin is one of the regions in the world exhibiting free-air anomalies that are predominately positive.

## FILTERED BATHYMETRY AND FREE-AIR GRAVITY ANOMALY MAPS

### Quantity and Distribution of Data Relative to Complexity of Structure and Bathymetry

The Panama Basin is a structurally complex region of the sea floor. In a  $14^{\circ}$  by  $16^{\circ}$  area from  $4^{\circ}\text{S}$  to  $10^{\circ}\text{N}$  latitude and from  $76^{\circ}\text{W}$  to  $92^{\circ}\text{W}$  longitude, there are several aseismic ridges, fracture zones, and centers of sea-floor spreading; there are two trenches, a marginal trough sequence, and a major graben. Besides conforming to these relatively long-wavelength structural features, the bottom is characterized by short-wavelength and high-amplitude topography over rather large areas.

In this region of the Eastern Equatorial Pacific, there are surface-ship tracklines represented by 19,673 depth values and 7,430 free-air gravity anomaly values. These tracklines, however, are not uniformly distributed (Figure 2). In the NOAA survey area, the basic trackline spacing is 56 km (30 nm), and the spacing is 28 km (15 nm) in a  $2\frac{1}{2}^{\circ}$  by  $2\frac{1}{2}^{\circ}$  area from  $4.5^{\circ}\text{N}$  to  $7^{\circ}\text{N}$  latitude and from  $81.5^{\circ}\text{W}$  to  $84^{\circ}\text{W}$  longitude. However, the major part of the basin is covered only by the OSU survey, for which the trackline spacing is 222 km (120 nm). Although there is a large amount of data to analyse, its distribution is insufficient to resolve the shorter-wavelength components of the structure and bottom topography in most of the basin.

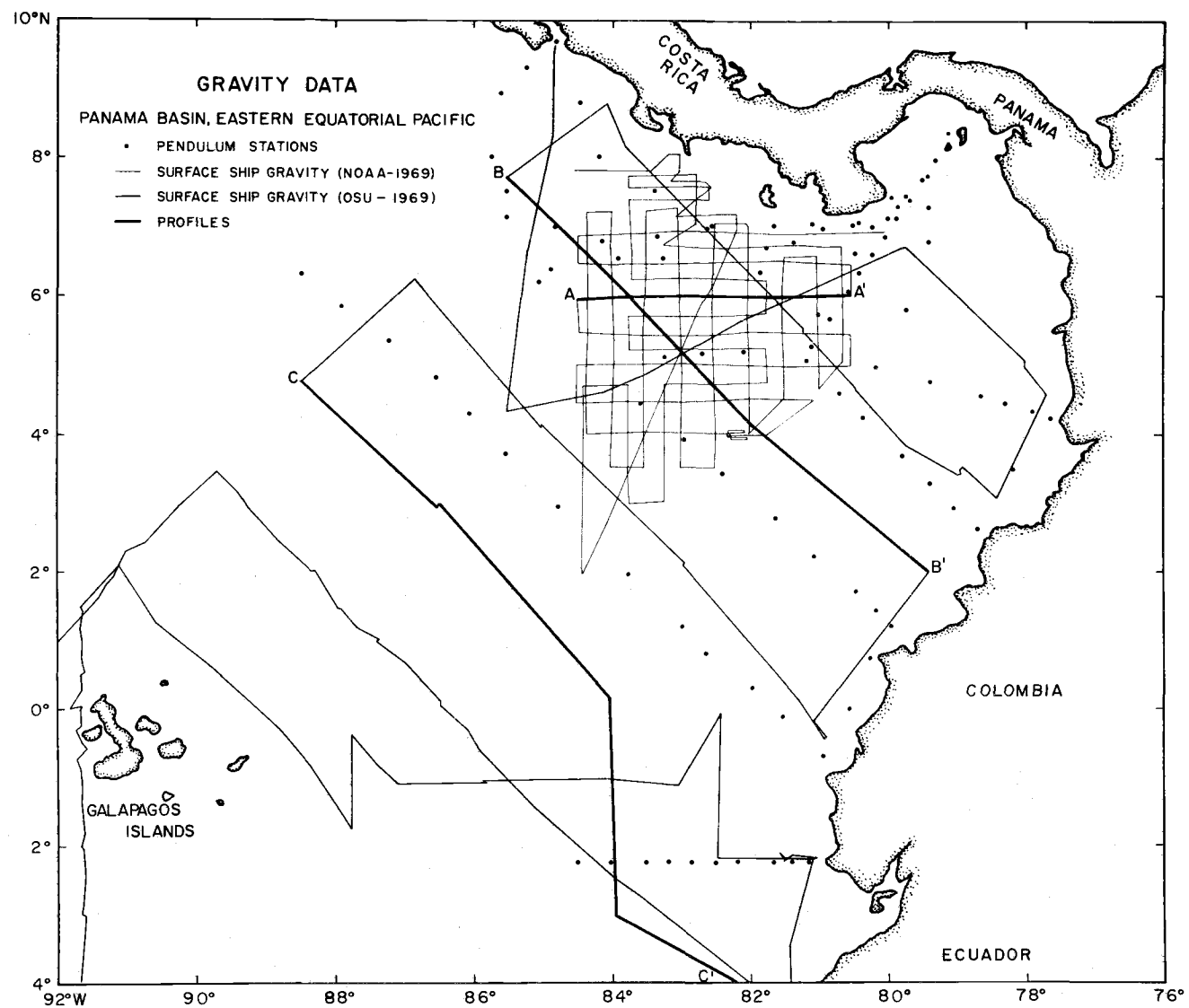


Figure 2. Location map of surface-ship gravity meter tracklines and submarine pendulum stations.

In response to these observations, a data-processing method was devised to 1) reduce the scope of the problems to be investigated, 2) optimize the spatial distribution of data relative to the wavelengths of the investigated problems, and 3) reduce the task of data analysis.

### Filtering of Surface-Ship Data

Because surface-ship geophysical data are seldom gridded or uniformly distributed, spatial filtering is a difficult and questionable procedure. From a theoretical point of view, it is best to use a low pass filter with a cutoff wavelength of at least twice the maximum data spacing. From a practical point of view, however, such a filter is in most cases too severe, resulting in the attenuation of important anomalies. Therefore, spatial filtering is sometimes a compromise between no filtering at all and that which is theoretically minimal. The following two-phase method is such a compromise.

#### Phase 1 -- Gridding and Averaging

In the first phase of filtering, a rectangular area from  $4^{\circ}\text{S}$  to  $10^{\circ}\text{N}$  latitude and from  $76^{\circ}\text{W}$  to  $92^{\circ}\text{W}$  longitude was divided into a 64 by 56 array of  $15'$  grid squares, and each square was assigned two indices numbered consecutively from the southwest corner of the grid. The X or longitude index was designated J, and the Y or latitude index

was designated K. An input file was then searched, and two 64 by 56 matrices were computed and stored on magnetic tape. The first matrix, designated  $N(J, K)$ , is an integer array of the number of input data values that are included by each grid square. The second matrix, designated  $D(J, K)$ , is a real array of the corresponding averages of the data values in each grid square.

The process was repeated three times; once for free-air gravity anomaly, once for magnetic anomaly, and once for bathymetry (Appendix 1). The resulting magnetic tape file contains an N and D array for each of these three data types.

As a result of phase 1, the input data file is converted into matrices, which can be thought of as representing a grid of filtered data values: one data value located at the center of each grid square.

The advantage of such a data set, being represented by matrices, is that it can be treated mathematically as a unit rather than as a set of isolated values.

The disadvantages of such a data set are two-fold. First, averaging data in 15' squares roughly corresponds to a low-pass filtering operation in which wavelengths shorter than 15' are filtered out of the data, thereby leaving wavelengths as short as 15' sampled with a 15' grid. Information theory requires that the sampling interval be no more than half the shortest wavelength in the data. Therefore, for a 15' grid, the averaging should take place over 30'

rather than 15' squares. Second, in the assignment of the averaged value to the center of the grid square, the distribution of the original data within the square is not taken into account.

In order to overcome these disadvantages, phase 2 is employed.

### Phase 2 -- Further Averaging and Coordinate Assignment

The second phase of filtering results in a 30' average for each compound square made up of four adjacent simple 15' grid squares. Figure 3a represents one compound square for which the computed average is

$$\frac{D(J, K)N(J, K) + D(J+1, K)N(J+1, K) + D(J, K+1)N(J, K+1) + D(J+1, K+1)N(J+1, K+1)}{N(J, K) + N(J+1, K) + N(J, K+1) + N(J+1, K+1)}.$$

It is important to note that this average is equivalent to the simple average of the original data included in the compound square.

A position is then assigned to the above average according to the following four cases, listed in the order of preference:

- Case 1 -- (Figure 3b) At least two diagonally opposed simple grid squares are non-empty. In this case, the assigned position is the center of the compound square.
- Case 2 -- (Figure 3c) Grid squares J, K and J, K+1 are non-empty, but J-1, K and J-1, K+1 are empty. In this case, the assigned position is the point midway between the centers of the two non-empty squares.
- Case 3 -- (Figure 3d) Grid squares J, K and J+1, K are non-empty, but J, K-1 and J+1, K-1 are empty. In this case, the assigned position is the point midway between the centers of the two non-empty squares.



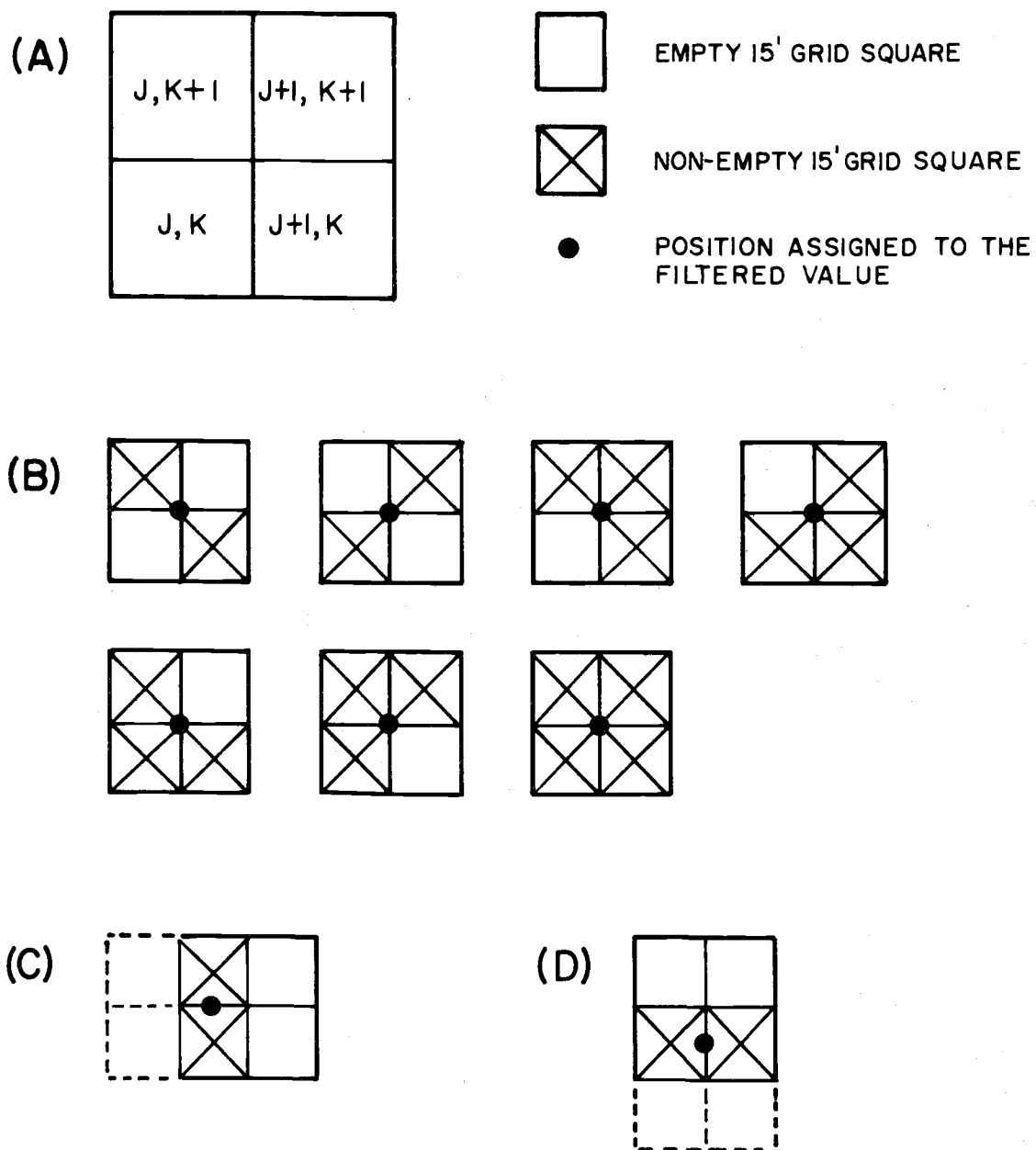


Figure 3. Diagram illustrating Phase 2 in the filtering of surface-ship data. (a) Compound square consisting of four adjacent simple grid squares, (b) Coordinate assignment Case 1, (c) Coordinate assignment Case 2, and (d) Coordinate assignment Case 3.

Case 4 -- Data fits none of the above three cases. In this case, no position is assigned, and the computed average does not appear in the file of filtered data.

This process is repeated for each value of J and K to arrive at a file of data that approximately represents an array of 30' averages, digitized at a 15' sampling interval.

### Example

In order to better explain the filtering method, the following example is presented:

Figure 4a is a map of the digitized free-air gravity anomalies representing a surface-ship trackline traversing the  $1^{\circ}$  square area whose southwest corner is at  $2^{\circ}\text{N}$  latitude and  $86^{\circ}\text{W}$  longitude.

Figure 4b is a diagram of the two corresponding arrays computed by the application of filtering phase 1. The indices range from 25 to 28 because the grid origin is at  $4^{\circ}\text{S}$  latitude and  $92^{\circ}\text{W}$  longitude. The array elements corresponding to empty grid squares [i. e. grid squares for which  $N(J, K)=0$ ] have been omitted to help clarify the explanation of filtering phase 2. The results of this second filtering phase are shown in Figure 4c. Comparison between this map of the filtered data and the diagram of the computed arrays shows that the 1-mgal and 2-mgal values are located according to case 1, the 4-mgal value is located according to case 2, and the -5-mgal value is located according to case 3.

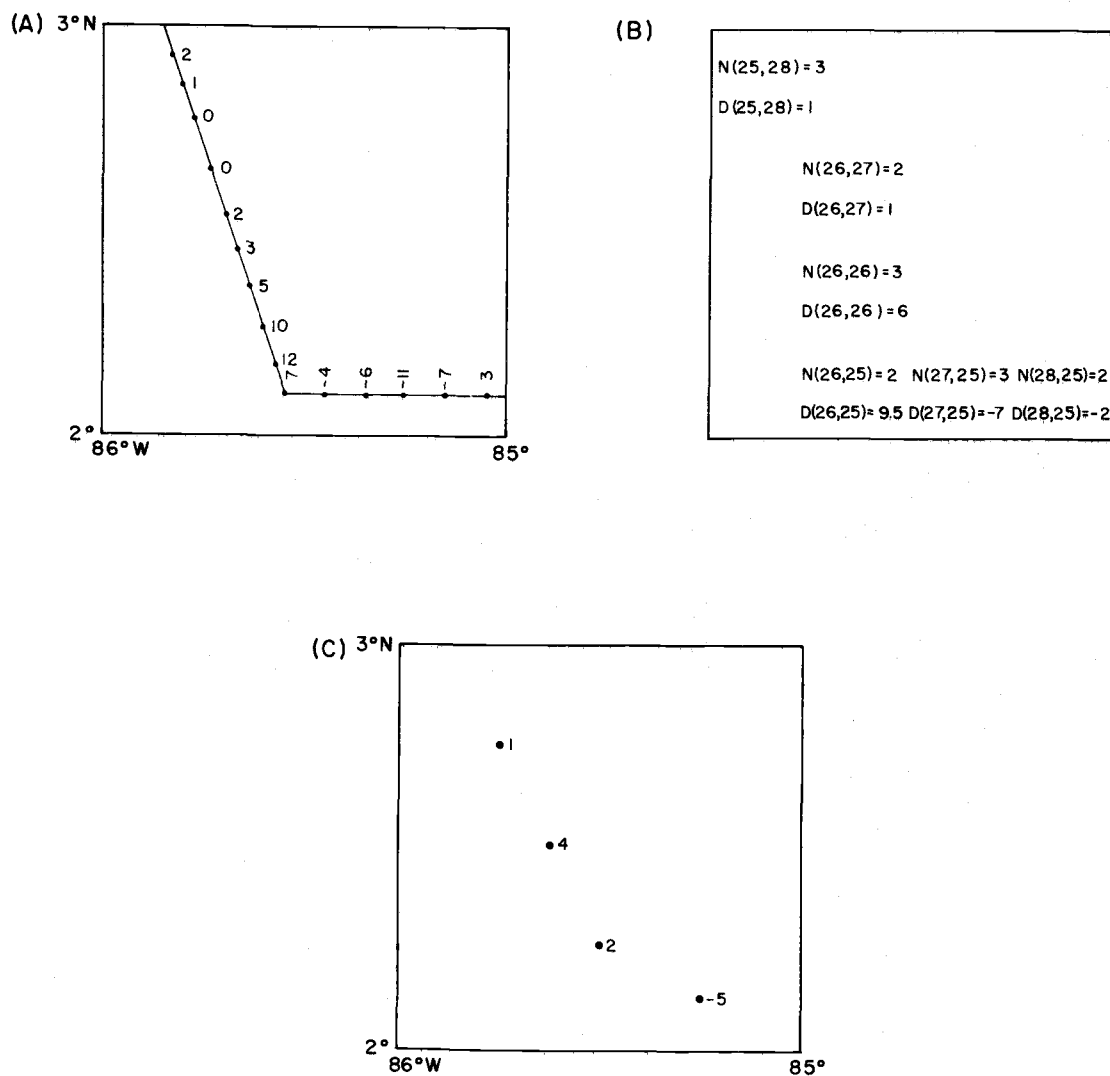


Figure 4. Example of the method used to filter bathymetry and free-air gravity anomalies. (a) Surface-ship gravity data, (b) N and D matrix elements computed by filtering Phase 1, and (c) Filtered gravity data computed by filtering Phase 2.

### Maps Construction

The file of filtered surface-ship data was plotted on mercator charts along with the data from 115 pendulum stations. The resulting base maps were contoured, ignoring all pendulum station data located within 28 km (15 nm) of filtered data values and giving equal weight to all other data points.

### Discussion of Maps

Because of the limitations imposed by the non-uniform distribution of data and the filtering method followed, the only part of these maps that is adequately defined is the  $2\frac{1}{2}^{\circ}$  by  $2\frac{1}{2}^{\circ}$  area of the NOAA survey for which the trackline spacing is 28 km, one-half the cutoff wavelength of the filter. Furthermore, the equal weighting of unfiltered pendulum station data and filtered surface-ship data leads to features that are clearly artificial. In spite of these difficulties, however, the maps are internally consistent, and the filtered bathymetry map compares favorably to the bathymetric contour map of van Andel et al. (1971a).

### Filtered Bathymetry Map

Figure 5 is a map of the filtered bathymetry. Although there is general agreement between it and the bathymetric contour map of

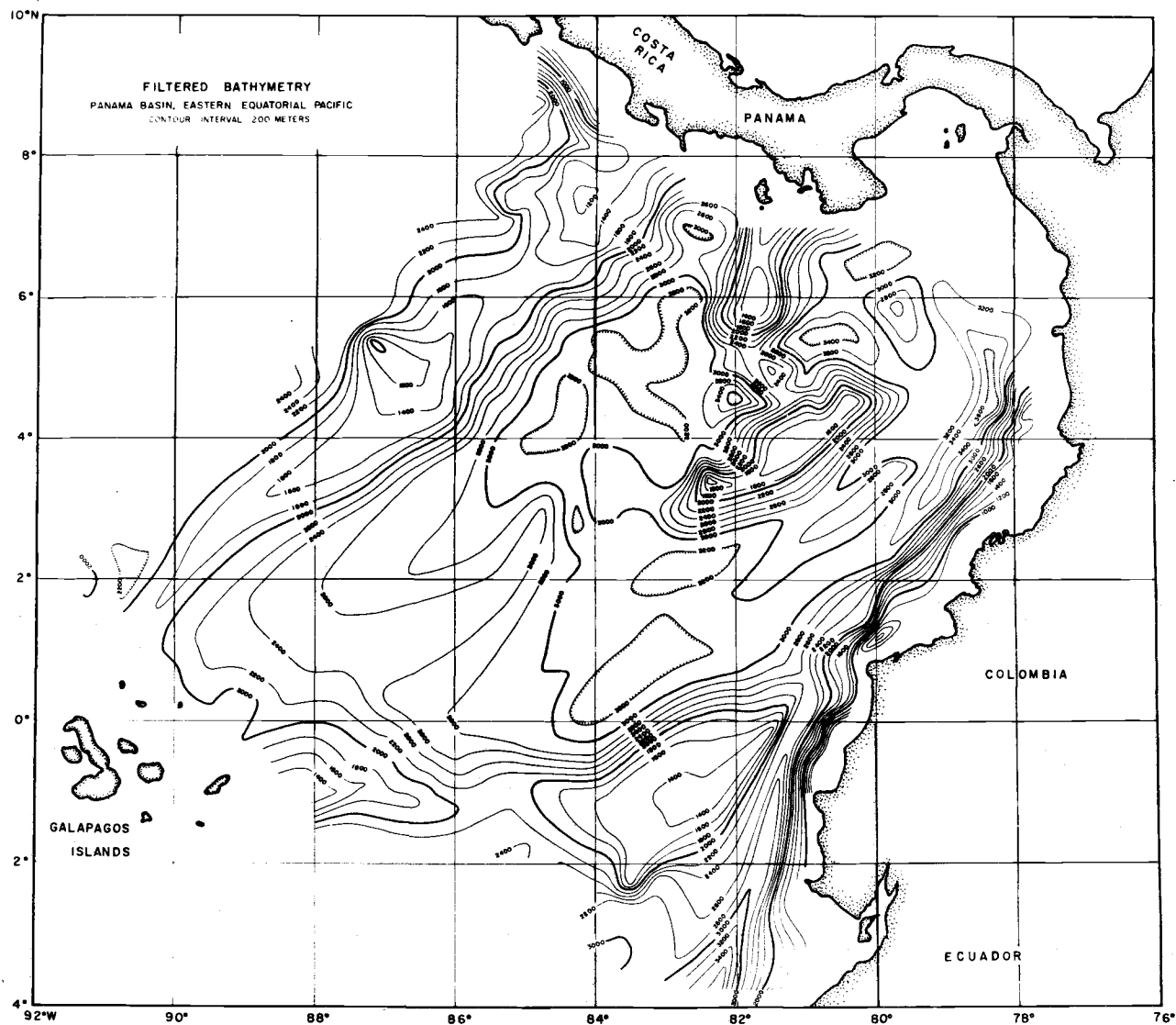


Figure 5. Map of filtered bathymetry.

van Andel et al. (1971a), there are two significant discrepancies.

The first is an apparent ridge on the filtered map trending northeast from  $1^{\circ}\text{N}$  latitude,  $87^{\circ}\text{W}$  longitude to  $3^{\circ}\text{N}$  latitude,  $85^{\circ}\text{W}$  longitude. This feature, which shows up best in the 2600-m contour, is controlled by data from only two tracklines and one pendulum station at its northeast end (Figure 2). Therefore, its simple shape is probably an artifact of insufficient data coverage. Because both fracture zones and centers of sea-floor spreading are normally expressed by bathymetric ridges, the northeast-trending ridge probably reflects and should, therefore, follow the stair-step pattern of east-west rift zone segments and north-south transform faults found in the western basin. This conclusion is strongly supported by the occurrence of a well-known fracture zone located at the point where Profile CC' (Figure 13) crosses the mapped ridge.

The second discrepancy between Figure 5 and the bathymetric contour map of van Andel et al. (1971a) is an apparent trough on the filtered map connecting deep areas of the eastern and western basins. Parallelling the coast at  $2^{\circ} 30'\text{N}$  latitude,  $80^{\circ} 30'\text{W}$  longitude and delineated by the 3000-m contour, this trough was contoured as shown because it is the simplest geometry consistent with the existing data. However, the fact that there is no data at this latitude between  $80^{\circ}\text{W}$  and  $81^{\circ}\text{W}$  longitude permits a north-south ridge less than 2800 m deep to breach the trough between these longitudes. Although this

alternate interpretation results in a more complex geometry, the resulting ridge conforms closely to the uplifted flanks of the Yaquina graben, contoured in the unfiltered map. As shown in Profile BB' (Figure 12), the central downfaulted block of the graben is less than 25 km wide, and the associated uplift is approximately 100 km wide. Therefore, on the filtered bathymetry map, the graben appears as a ridge.

Another suspicious-looking constriction in the region of the basin having a depth greater than 3000 m is a north-south trough, which connects the northern and southern portions of the western deep and separates the northeast-trending ridge discussed above from a lobate westward extension of the Malpelo ridge. This trough is probably real, marking the location of a fracture zone at  $84^{\circ}30'W$  longitude (Sclater and Klitgord, 1973). In the terminology of Grim (1970b), this trough coincides with the Equador fracture zone, the 3200-m closure in its center coincides with the 4200-m Equador depression, and the lobate western extension of the Malpelo ridge corresponds to the Costa Rica rift zone.

The Panama Basin is divided into three physiographic provinces by the Panama fracture zone at  $82^{\circ}30'W$  longitude and the fracture zone at  $85^{\circ}20'W$  longitude (Sclater and Klitgord, 1973). East of the Panama fracture zone, the bathymetry is quite complex with depths ranging from less than 1400 m for the Coiba ridge to greater than

3600 m seaward of the continental shelf at  $5^{\circ}\text{N}$ . Between the fracture zone at  $85^{\circ}20'\text{W}$  longitude and the Panama fracture zone, the bottom is predominantly deeper than 3000 m and generally conforms to the normal depth-age relationship of Sclater et al. (1971). West of the fracture zone at  $85^{\circ}20'\text{W}$  longitude, the bottom is predominantly less than 3000 m deep and in some places is as much as 1 km shallower than the depth predicted by Sclater's curves.

The Cocos, Carnegie, Coiba, and Malpelo aseismic ridges are all represented by depths shallower than 2000 m. Other than the continental margin, these are the only areas in the basin that are this shallow.

The Peru-Chile trench, extending northward into the survey area at  $82^{\circ}\text{W}$  longitude, is well represented by depths as low as 3400 m. The Middle America trench, however, is not apparent on the filtered map.

#### Filtered Free-Air Gravity Anomaly Map

Figure 6 is a map of the filtered free-air gravity anomalies. The significant features of this map are discussed below.

Free-air anomalies less than -20 mgal are confined for the most part to a belt adjacent to the coastline. This near-short negative anomaly belt is interrupted only at two places. In the bend around the Gulf of Panama, this feature is interrupted by a zone of no data.



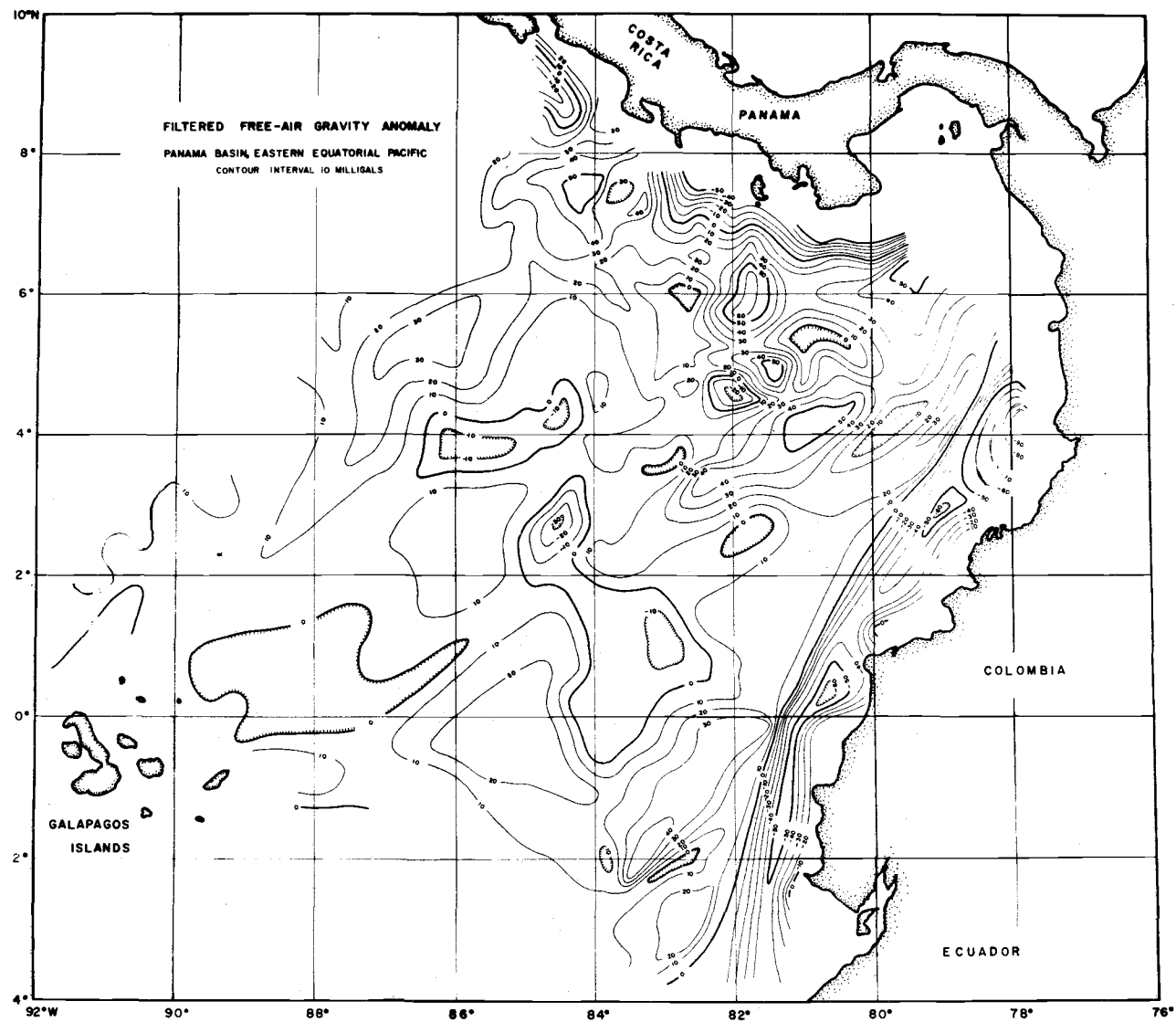


Figure 6. Map of filtered free-air gravity anomalies.

Hayes (1966), however, shows that the negative anomaly belt is continuous throughout this zone. The interruption at the intersection of this feature with the Cocos ridge, however, is clearly real as indicated by the fact that the gravitational signature of the Middle America trench is completely truncated by the +20-mgal contour.

Other than the negative anomaly belt discussed above, there are only two small areas in the Panama Basin where the free-air anomaly is less than -20 mgal. One at  $4^{\circ}30'N$  latitude,  $82^{\circ}W$  longitude corresponds to a bathymetric depression to depths greater than 3600 m (Figure 5). The other at  $2^{\circ}45'N$  latitude,  $84^{\circ}30'W$  longitude corresponds to the Ecuador depression mentioned above. On the unfiltered free-air anomaly profiles of Barday (1971), this depression is manifested by a -70-mgal anomaly.

Free-air anomalies greater than +20 mgal form a semi-continuous band just seaward of the negative anomaly belt discussed above. The continuity of this band is interrupted at only three places: at  $3^{\circ}30'S$  latitude by a northeast-trending fracture zone, at  $2^{\circ}S$  latitude by a northeast-trending negative anomaly at the foot of the Carnegie ridge, and between the equator and  $3^{\circ}N$  latitude by a broad zone extending east-west across the entire basin and containing no anomalies less than -20 mgal or greater than +20 mgal. The slope and amplitude of the gravity anomaly associated with the southeastern boundary of the Carnegie ridge, at  $2^{\circ}S$  latitude, is the result of two

closely spaced pendulum stations with free-air anomalies of +47 and -6 milligals.

The most striking feature of the free-air anomaly map is a 200-km by 200-km area characterized by anomalies greater than +20 mgal and bounded on the north and east by the negative anomaly belt, on the west by the Panama fracture zone, and on the south by  $3^{\circ}$ N latitude. Although this area contains anomalies less than +20 milligals, these anomalies occupy a very small percentage of the total area. Furthermore, the boundary between this area and the zone of moderate free-air anomalies to the south is quite sharp, suggesting a major structural discontinuity in the eastern basin at  $3^{\circ}$ N latitude.

The remaining area characterized by free-air anomalies greater than +20 mgal is the landward half of the Cocos and Carnegie ridges. On the Carnegie ridge, the apparent northward extension of the +20-mgal contour at  $85^{\circ}$ W longitude is based on only one point. If this point had been rejected, as it was for the filtered bathymetry map, then these maps would be conformal, and the +20-mgal contour would not extend north of the equator.

Anomalies greater than +40 mgal correspond to the extreme landward ends of the Cocos and Carnegie ridges and the aseismic, abnormally shallow structures of the eastern basin.

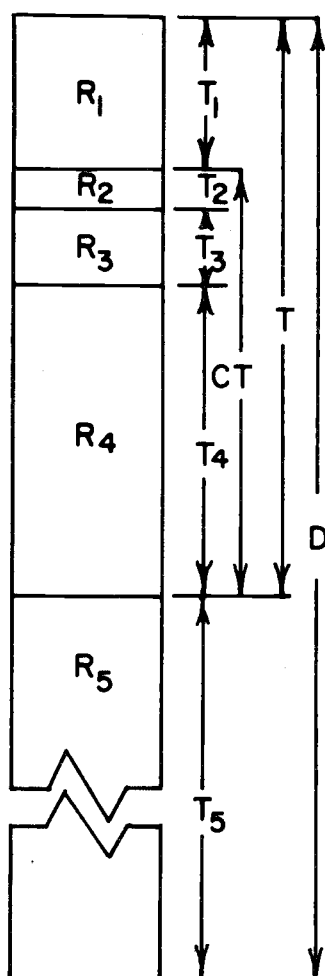
Finally, the entire western basin, like the southern half of the eastern basin, is characterized by moderate gravity anomalies. At  $4^{\circ}45'N$  latitude,  $82^{\circ}30'W$  longitude, there is a small area where the free-air anomaly is greater than +20 milligals; and, as stated above, at  $2^{\circ}45'N$  latitude,  $84^{\circ}30'W$  longitude, the Equador depression is expressed by a -30-mgal low. Everywhere else the free-air anomaly is less than +20 mgal and greater than -20 mgal.

## ASSUMPTIONS MADE IN THE CONSTRUCTION OF CRUSTAL MODELS

Construction of crustal models from gravity data at best yields non-unique results. Lack of seismic refraction control to remove some of the inherent ambiguities necessitates many restrictive assumptions, which can best be discussed in reference to Figure 7. This figure includes a diagram of an infinite-slab model, a key giving the definitions of associated variables, and a list of the equations relating these variables. Of the 16 variables listed, five can be determined from the given equations, and the following four are known:  $R_1=1.03$ , the average density of sea water;  $T_1$ =measured depth;  $T_2$ =sediment thickness measured from isopach map (van Andel *et al.*, 1971a);  $G$ =measured free-air gravity anomaly. Therefore, seven indeterminate variables remain to be resolved by the following five assumptions:

### No Significant Lateral Changes in Density Take Place Below a Depth of 50 KM

The fact that standard sections of 50 km and shallower have been used successfully for all seismically controlled crustal models, except those over active trenches (Appendix 2), indicates that the above assumption is justified for the Panama Basin survey area, which contains only the terminal ends of the Middle America trench and the



$R_1, T_1$  : DENSITY AND THICKNESS OF WATER LAYER

$R_2, T_2$  : DENSITY AND THICKNESS OF SEDIMENT LAYER

$R_3, T_3$  : DENSITY AND THICKNESS OF TRANSITION LAYER

$R_4, T_4$  : DENSITY AND THICKNESS OF OCEANIC LAYER

$R_5, T_5$  : DENSITY AND THICKNESS OF UPPER MANTLE

CT : CRUSTAL THICKNESS EXCLUDING WATER DEPTH

T : DEPTH TO MANTLE

G : FREE-AIR GRAVITY ANOMALY

AT : GRAVITATIONAL ATTRACTION OF THEORETICAL MODEL CORRESPONDING TO ZERO FREE-AIR ANOMALY

AC : GRAVITATIONAL ATTRACTION OF COMPUTED MODEL

$$CT = \sum_{i=2}^4 T_i \quad (1)$$

$$T = CT + T_1 \quad (2)$$

$$D = T + T_5 \quad (3)$$

$$G = AC - AT \quad (4)$$

$$AC = K \left( \sum_{i=1}^5 R_i T_i \right) \quad (5)$$

WHERE  $K = 2\pi\gamma$  -- CONSTANT USED TO COMPUTE THE ATTRACTION OF AN INFINITE SLAB

Figure 7. Diagram and equations for infinite-slab model.

Peru-Chile trench. Further justification of this assumption is implied by the apparent absence of ultra-long-wavelength components in the Panama Basin gravity field.

Implicit in the justification of the use of all standard sections and, hence, arguments for isostatic compensation at some fixed depth, is the reasonableness of the computed cross sections. Significant lateral changes in density below the computed section could very well lead to unreasonable densities when the model is constrained by seismic refraction stations. However, in a locale such as the Panama Basin where there is little or no constraint placed on the deep structure, the breakdown of this assumption cannot be detected. That the computed depth of the Mohorovicic discontinuity might exhibit a long-wavelength error is about all that can be said under these circumstances.

The Densities of the Crustal Layers Are Equal to  
Those of the Standard Section

That three crustal layers exist has already been assumed in the construction of Figure 7. This assumption is supported by data from the majority of marine seismic refraction stations, although according to Shor et al. (1970) there are definite indications, especially north of Hawaii, that there are actually four layers. Similarly, the majority of crustal models have been computed on the basis of three layers,

but a few (Talwani et al. 1959b; Couch, 1969) have been computed on the basis of four.

That these layers have constant densities equal to those of the standard section is the conventional assumption in areas where seismic refraction results do not present contradictory constraints. This convention is based on seismic refraction data (Shor et al. , 1970), which show that crustal thickness is more variable than crustal density.

How reasonable this assumption is can best be assessed by looking at Figure 8. The densities of the computed standard section (Appendix 2) are 2.0 for the sediment layer (layer 1), 2.6 for the transition layer (layer 2), and 2.9 for the oceanic layer (layer 3). These densities certainly fall within the ranges of the corresponding density distributions shown in the figure. Given the scatter in the densities of the transition layer, it appears that the assumption of constant density is most in error when applied to this layer. However, the resulting error is second in magnitude to that caused by the assumption made below that the thickness of the transition layer is constant.

The Density of the Upper Mantle is Constant  
to a Depth of 50 KM

From Figure 8, it appears that this assumption is as good as the previous assumption about the densities of the crustal layers.



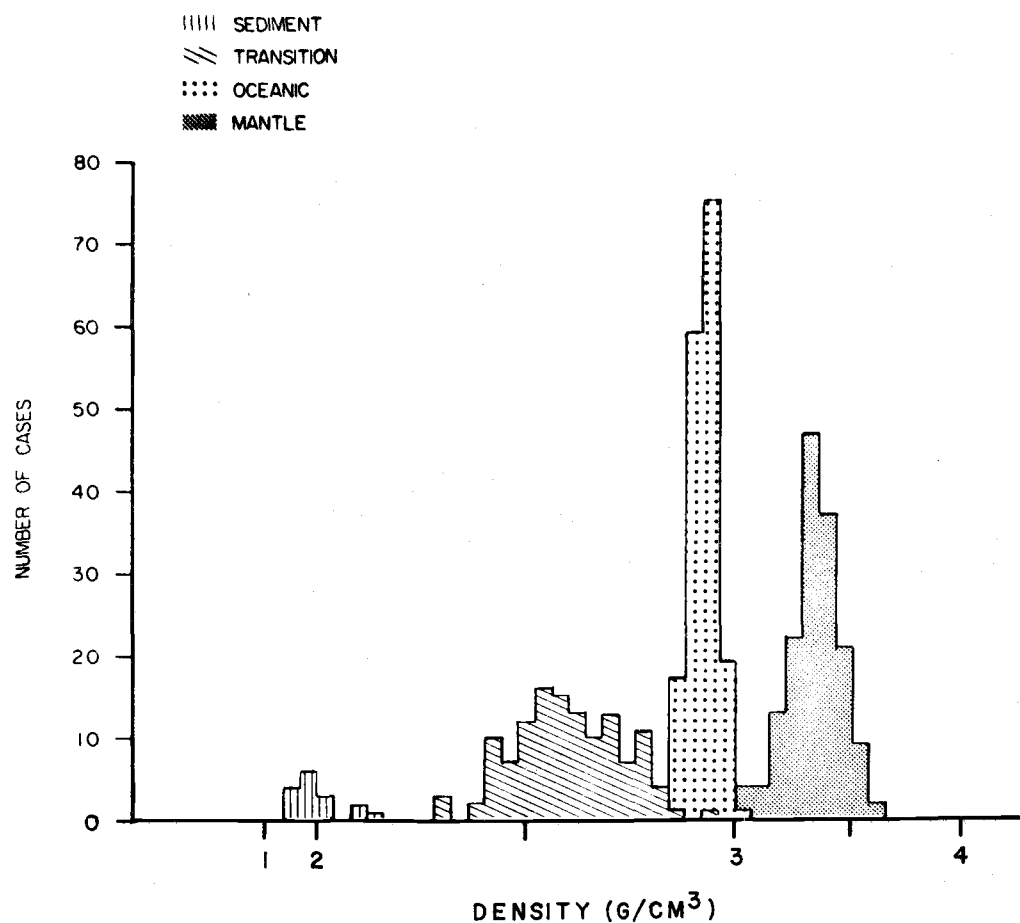


Figure 8. Diagram illustrating the distribution of densities for the sediment, transition, oceanic, and mantle layers. This figure is the velocity distribution given by Shor *et al.* (1970) with the abscissa relabeled as density according to the Ludwig, Nafe, and Drake (1970) curves.

However, there are two reasons why this is the most limiting assumption of all: 1) In a 50-km marine section with approximately 40 km of mantle, a  $0.01\text{-g/cm}^3$  change in mantle density causes a 17-mgal change in the attraction of an infinite slab. Therefore, the mantle density is an order of magnitude more critical than the crustal densities. 2) There are petrologic and geophysical reasons why the density of the upper mantle is not constant.

An argument in favor of this assumption, in addition to its being necessitated by the absence of refraction control, is its apparent ability to yield reasonable results.

Although this assumption does not permit direct reduction in the number of indeterminate variables, it paves the way for later computations and permits construction of two- and three-dimensional models without necessitating additional assumptions.

The Thickness of the Oceanic Layer is Normal in Regions  
Undergoing Active Spreading, Exclusive of  
Aseismic Ridges

Normal thickness of the oceanic layer, according to Goslin et al. (1972), is given by  $T_3 = 5.05 - 1.805 \exp(-\text{age}/18)$ , where  $T_3$  is expressed in km and age is expressed in m.y. This relationship is depicted in Figure 9. It is interesting to note here that Goslin et al. (1972) also find no significant variation in the thickness of layer 3 with spreading rate.

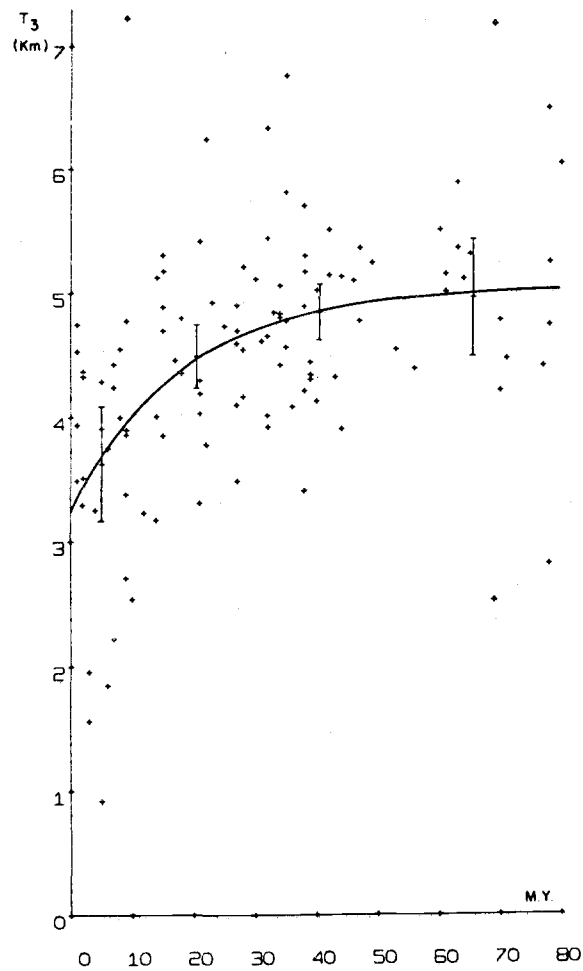


Figure 9. Thickness of the oceanic layer with age from Goslin et al. (1972).

That this relationship holds for a region as anomalous as the Panama Basin is subject to question. However, if it does hold, it does so in the western basin where the age of the crust is known from magnetic anomalies and the depth is close to that predicted by the empirical depth-age relationship of Sclater et al. (1971).

In conjunction with the assumption of constant upper mantle density, this assumption permits the computation of the mantle density.

#### The Thickness of the Transition Layer is 1.1 KM

Shor et al. (1970) argued for an inverse relationship between the spreading rate and the thickness of layer 2. Such a relationship is based on the physical reasoning that the discharge of lava at ridge crests is constant everywhere. Pictured in Figure 10a, the best fit to a limited set of data from the Pacific Ocean, Atlantic Ocean, Indian Ocean, and Red Sea is a curve representing a discharge rate of  $66 \text{ km}^3/10^6 \text{ yr}$  per kilometer of ridge crest.

Goslin et al. (1972) argued for a constant thickness of layer 2 with age (Figure 10b). They further argued that all the Pacific refraction data presented by Shor et al. (1970) only weakly suggest the inverse relationship proposed in Figure 10a, on the basis of fewer data points and supplemental data from three other areas.

As indicated by the dashed lines, both Figures 10a and 10b imply that a 1.1-km-thick layer is appropriate for a crust spreading

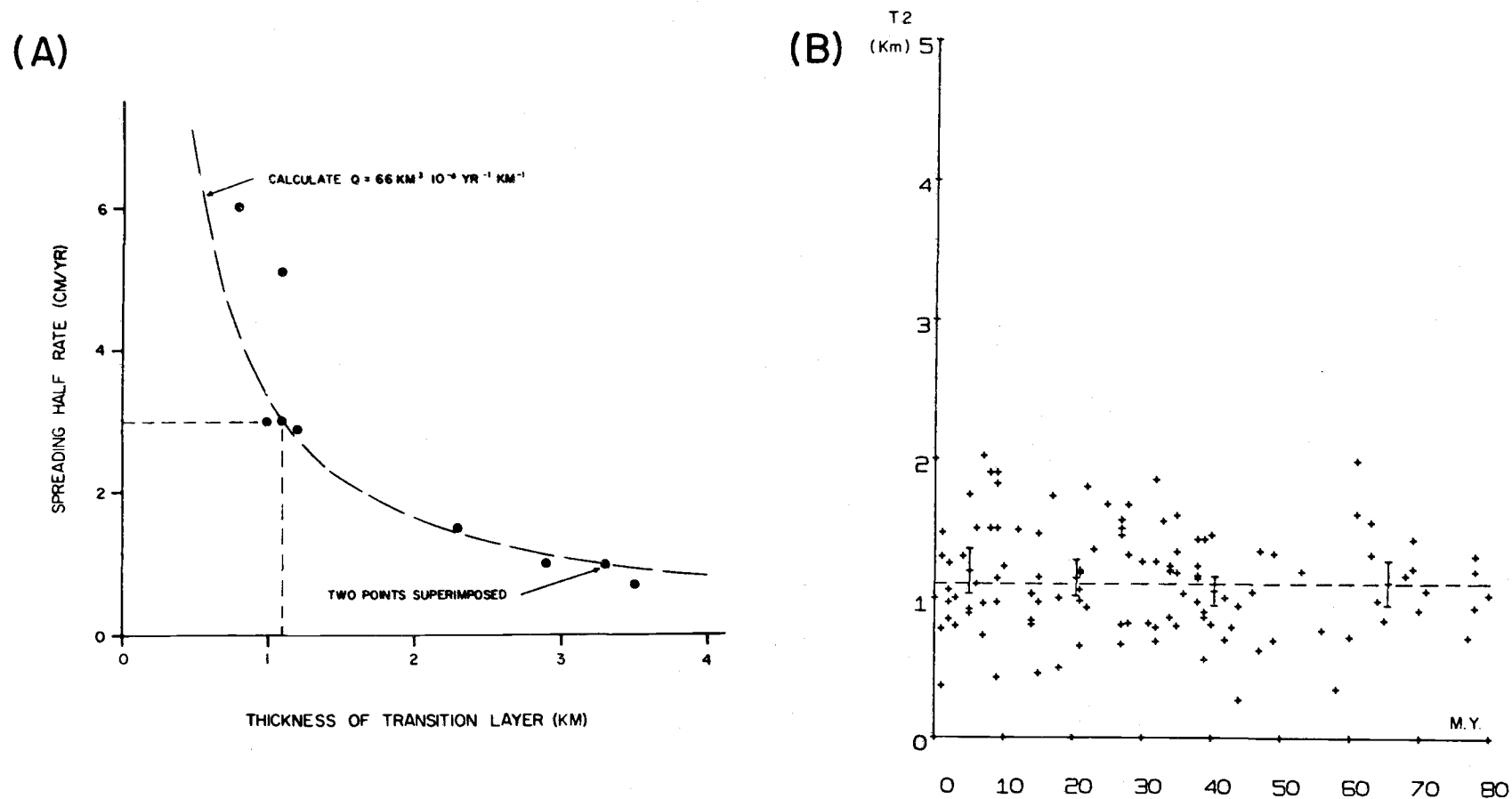


Figure 10. Diagram illustrating the argument for a constant 1.1-km thickness for the transition layer. (a) Spreading half-rate as a function of thickness of the transition layer as given by Shor et al. (1970). (b) Thickness of the transition layer with age as given by Goslin et al. (1972).

at a rate of 3 cm/yr. However, Shor et al. (1970) stated that the median thickness of layer 2 is 1.2 km rather than 1.1 km, which appears to be a better fit to the data presented in Figure 10b.

It should be emphasized that local variations in the thickness of layer 2 are not ruled out by the above work. The scatter in the data itself points to this conclusion. Shor et al. (1970) pointed out that although some of this scatter results from the inaccuracy in the determination of the layer velocity, much of it is probably real. They further stated that this is the most variable layer in the oceanic crust, and regional variations are evident. The fact that this variability is not taken into account leads to high-amplitude, short-wavelength errors in the Mohorovicic discontinuity of the crustal sections.

## CRUSTAL SECTIONS

### Determination of Mantle Density and Construction of Crustal Sections

Crustal sections are computed following the technique described by Talwani et al. (1959a), which is based on the assumption that structures are two-dimensional, extending to infinity in each direction normal to the given profiles. Therefore, profiles were selected to not only provide crustal cross sections of but also run transverse to the following physiographic and tectonic features (Figure 1): Profile AA'--Panama fracture zone and Coiba ridge; Profile BB'--Cocos ridge, Malpelo ridge, Yaquina graben, and marginal trough; Profile CC'--Cocos ridge, Carnegie ridge, and Peru-Chile trench.

The assumptions and equations discussed above essentially fix all the model variables except the thickness of the oceanic layer or the mantle density. However, the mantle density can be determined by applying the assumptions of normal oceanic layer thickness and constant mantle density as constraints on the computed sections.

Since the standard section is determined for an oceanic crust with normal upper mantle density, the above constraint of normal oceanic layer thickness must be applied only to those parts of the profiles at which there is expected to be both normal oceanic crust and normal upper mantle. Normal oceanic crust, as mentioned in

the argument for normal oceanic layer thickness, is expected to be found only in the triangular area of the Panama Basin that is bounded by the Cocos ridge, the Carnegie ridge, and the Panama fracture zone. On the other hand, normal upper mantle, according to Shor et al. (1970), is found at distances greater than 250 km from active spreading centers. Therefore, only a very small area of the Panama Basin is left in which to apply the above constraints. Figure 1 shows that this area is spanned by profiles AA' and BB' in the distance ranges listed in Table 1.

Based on preliminary calculations using the infinite-slab approximation, the crustal sections were computed using a mantle density of  $3.28 \text{ g/cm}^3$  ( $0.04 \text{ g/cm}^3$  less than the standard section). Measured from these sections, the approximate thickness of layer 3 in the area of normal crust and subcrust is listed in Table 1. An approximate average of this thickness is 4.5 km.

Since the age of the crust in this area is approximately 9 m. y., the thickness of the oceanic layer should be 4.0 km, according to the formula of Goslin et al. (1972). The thickness of the oceanic layer computed with a mantle density of  $3.28 \text{ g/cm}^3$  is, therefore, 0.5 km too great. However, a mantle density of  $3.27 \text{ g/cm}^3$  would be even more anomalous and would result in a computed thickness of the oceanic layer 0.5 km too small. Therefore,  $3.28 \text{ g/cm}^3$  is the most conservative choice for the mantle density, based on the assumptions



Table 1. Computed oceanic layer thickness in region of normal oceanic crust and subcrust.

Profile	Distance	Thickness
AA'	100 - 200	5.0 - 4.0
BB'	280 - 350	5.5 - 3.5

Approximate average thickness of oceanic layer in area of normal oceanic crust and subcrust 4.5 km

Distance = profile distance spanned by region of normal oceanic crust and upper mantle

Thickness = approximate thickness of oceanic layer with a mantle density of  $3.28 \text{ g/cm}^3$

discussed above and the convention of rounding mantle density off to the nearest hundredth.

The  $0.04\text{-g/cm}^3$  difference between the mantle density of the standard section and that of the crustal models can be entirely accounted for by phase changes and thermal expansion in the lithosphere. The area of normal oceanic crust and subcrust spanned by profiles AA' and BB' corresponds to a crustal age of approximately 9 m. y., whereas the standard section is determined for a patch of oceanic crust with an age of approximately 25 m. y. In the lithospheric model of Sclater and Klitgord (1973, Figure 14),  $0.01\text{ g/cm}^3$  is accounted for by the shoaling of the Plagioclase-to-Pyroxene phase change, and  $0.03\text{ g/cm}^3$  is accounted for by an average lithospheric temperature change of  $225^\circ\text{C}$  between 9 m. y. and 25 m. y.

Finally, the crustal sections were constructed by rigidly adhering to assumptions of a constant mantle density of  $3.28\text{ g/cm}^3$ , constant crustal densities equal to those of the standard section, and a constant thickness of layer 2. This later assumption was violated only at one location landward of the Peru-Chile Trench on Profile CC'.

### Crustal and Subcrustal Cross Sections

The most striking feature of the crustal sections presented in Figures 11 through 13 is the jagged appearance of the Mohorovicic

discontinuity. The primary causes of this short-wavelength, high-amplitude noise are variations in the thickness of the transition layer and departures of the sediment-layer thickness from that shown on the isopach map of van Andel et al. (1971a). In the construction of these crustal sections, only the crust-mantle interface is adjusted to account for the observed free-air gravity anomaly. Therefore, residual variations in the thickness of layers 1 and 2 must be compensated for by similar variations in the crust-mantle interface. Furthermore, because of downward continuation effects, the resulting variations in the Mohorovicic discontinuity are amplified by an amount that is exponentially related to the depth difference between these shallow layers and the crust-mantle interface, divided by the wavelength of the residual variations.

Because the crustal sections are computed from the original unfiltered data based on the assumption of two-dimensionality, the modeled Mohorovicic discontinuity departs from that computed from the filtered data using the infinite-slab approximation, especially in areas where the crust-mantle interface exhibits short-wavelength, high-amplitude changes. Here, the mapped discontinuity is smoother and of lower amplitude than that of the crustal sections. In most places, however, the agreement between the two is very good.

In view of the above observations, the best estimate of the true location of the Mohorovicic discontinuity is probably a smoothed

version of the profiled interface. Therefore, the depths to the crust-mantle interface quoted in the following discussion of the individual profiles are estimates of the depth to such a smoothed interface.

The distances referred to in the following discussion are measured along the profiles from their left or western ends.

### Profiles AA'

Represented in Figure 11, Profile AA' provides crustal and subcrustal cross sections of three major structural features.

From 0 km to 100 km, the Cocos ridge rises to a depth of 1.9 km, is expressed by a free-air anomaly of +46 mgal, and is underlain by a Mohorovicic discontinuity as deep as 13.5 km. Similarly, from 270 km to 385 km, the Coiba ridge rises to a depth of 0.9 km, is expressed by a free-air anomaly of +89 mgal, and is underlain by a Mohorovicic discontinuity as deep as 17.5 km, 2 km deeper than the mapped depth.

Between these two ridges, from 100 km to 270 km, however, the structure isn't as straight forward. Here, the bathymetry is characterized by a graben-like normal faulting to a central low block 4.65 km deep. Over this block the free-air anomaly is -46 mgal, and beneath it the Mohorovicic discontinuity reaches a minimum depth of 8.5 km, 1 km less than the mapped depth. Based on the location of earthquake epicenters and the termination of east-west magnetic

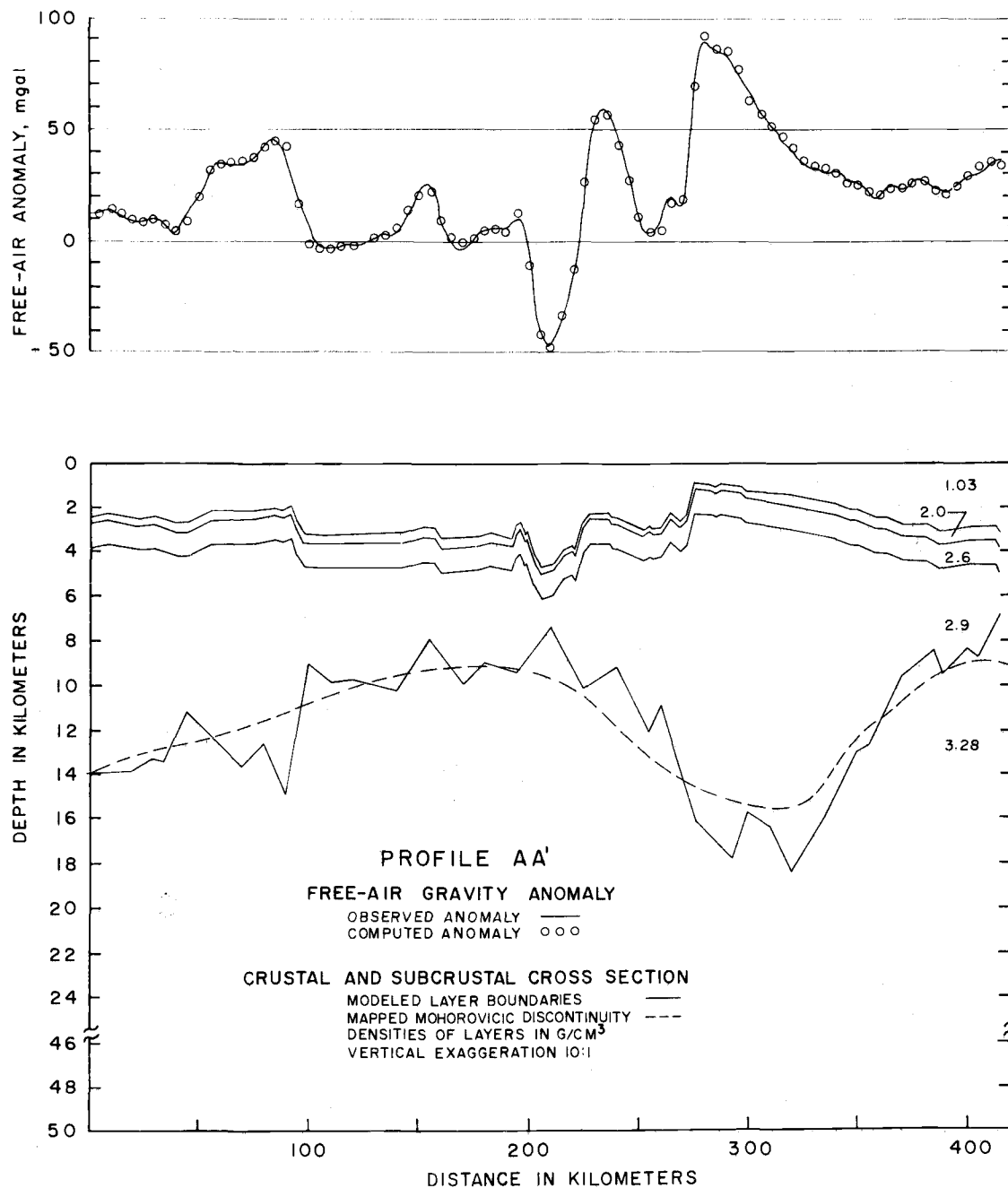


Figure 11. Crustal and subcrustal cross section for free-air gravity anomaly Profile AA'.

anomalies at its western boundary fault, the central block is the locus of the Panama fracture zone. On either side of this block there are two or more downfaulted blocks, each of which slopes away from the fracture zone. However, the net effect of the downfaulting is an increasing depth from each aseismic ridge to the fracture zone. This increase in depth and the resulting shoaling of the Mohorovicic discontinuity is exactly opposite to what is observed for the fracture zones in the rest of the basin and most fracture zones elsewhere (cf. van Andel et al., 1971b; Menard and Atwater, 1969).

Perhaps this apparent enigma is caused by the proximity of the aseismic ridges. Although both ridges appear to be terminated by normal faults with greater than 1 km of displacement, perhaps these ridges actually extend to the fracture zone and, therefore, their relief dominates and overrides this feature. This speculation is supported by the apparent width of the aseismic ridges on the other two profiles. If this is true, however, the computed mantle density should be greater and the crust thicker everywhere since, for the purpose of computing mantle density, the section of Profile AA' between the eastern fault of the Cocos ridge and the Panama fracture zone (100 km to 200 km) is considered to overlie normal crust.

### Profile BB'

Represented in Figure 12, Profile BB' provides crustal and subcrustal cross sections of five major structural features.

Spanned by this profile, at least from 15 km to 285 km, the Cocos ridge reaches a minimum depth of 1 km, has an associated maximum free-air anomaly of +75 mgal, and lies above a mantle that reaches a depth of 17 km. Although the ridge appears to be terminated at the south by a large normal fault with over 1 km of relief, the bottom continues to slope away from the ridge until, at a distance of 374 km, it is 3.3 km deep. This slope is clearly abnormal with respect to the depth-age relationship of Sclater et al. (1971), but whether or not normal crust underlies this area is subject to question. Since the segment of this crustal section from 280 km to 350 km is assumed to represent normal oceanic crust for the purpose of mantle-density determination, a negative answer to the above question would indicate a higher mantle density and a deeper crust.

The Panama fracture zone is reflected by a peak in the topography, at 456 km, to a minimum depth of 2.3 km and a free-air anomaly of +49 mgal. It is located near the center of a 95-km-wide topographic rise between two maximum depths of 3.7 km, at 409 km, and 3.6 km, at 504 km. Both the differential elevation of this rise and the associated depression of the Mohorovicic discontinuity are

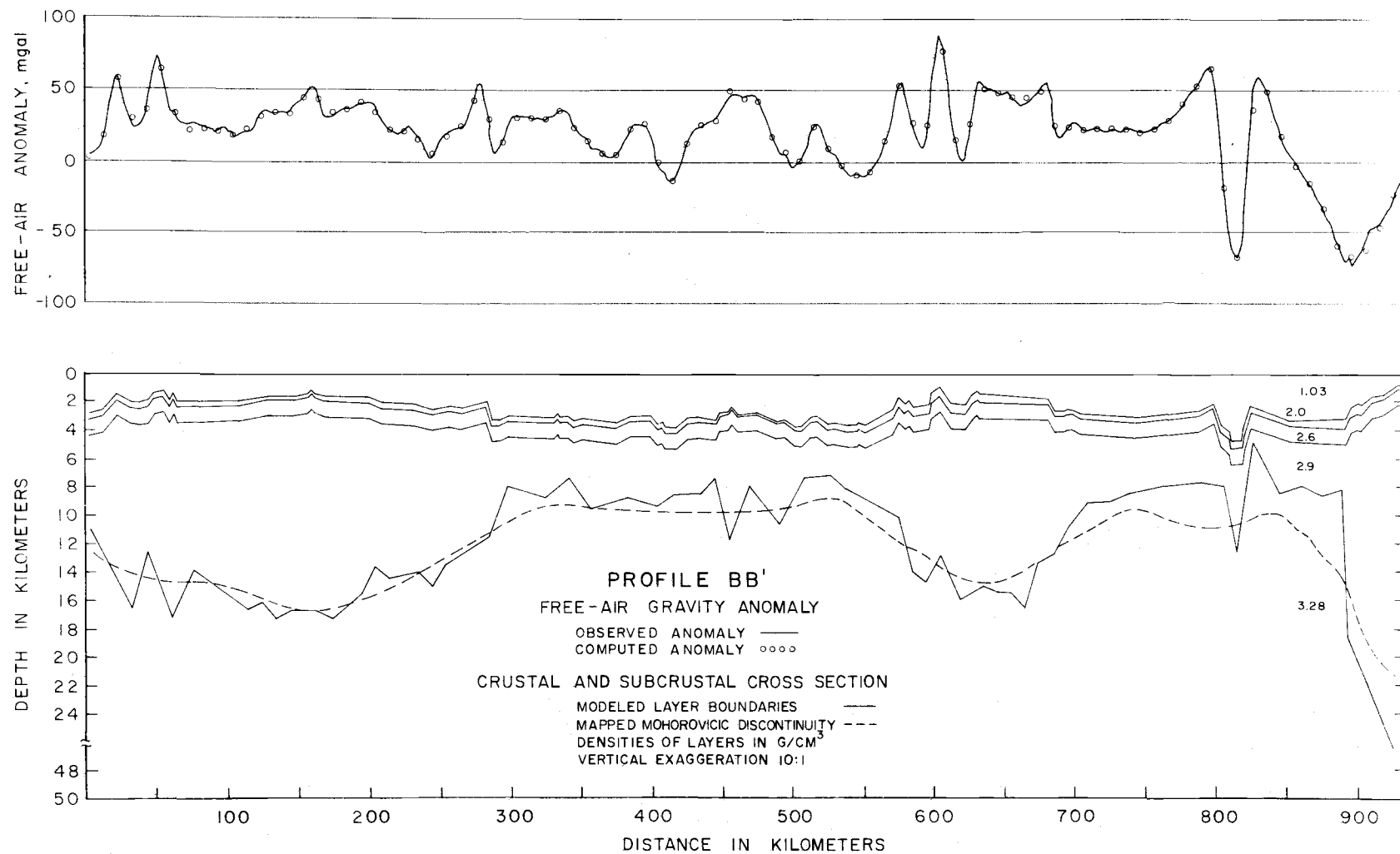


Figure 12. Crustal and subcrustal cross section for free-air gravity anomaly Profile BB'.



approximately 1 km. Thus, the fracture zone results in a 2-km thickening of the crust.

Between 504 km and 539 km, the crust-mantle interface shoals to a depth of 8 km, 1.5 km shallower than the mapped depth. From a depth of 3.6 km, at 539 km, the bottom begins to shoal, rising to a minimum depth of 0.9 km, at the high point in the Malpelo ridge. This aseismic ridge, which results in a maximum free-air anomaly of +90 mgal and a maximum crust-mantle-interface depth of 15.5 km (1 km deeper than the mapped depth), lies between the local depth maximum at 539 km and another at 734 km. The primary topographic signature of this ridge is not as easy to define as it is for the Cocos ridge, but it probably extends from a scarp at 570 km to approximately 710 km where the bottom becomes relatively smooth.

From the depth maxima of 3.0 km at 734 km and 3.3 km at 854 km, the bottom slopes upward rather uniformly to depths of 2.05 km and 2.25 km where the free-air anomalies are +68 mgal and +61 mgal, respectively. In the middle of this uniform uplift is a central downfaulted block whose center, at approximately 810 km, has a depth of 4.7 km and a free-air anomaly of -65 mgal. This feature, called the Yaquina graben, is expressed by a deepening in the crust-mantle interface of less than 1 km. Here, the departure between the mapped and the modeled Mohorovicic discontinuity is as great as 3 km because of the proximity of the continental edge.

At approximately 900 km, a free-air anomaly of -70 mgal is the gravimetric expression of a marginal trough.

#### Profile CC'

Represented in Figure 13, Profile CC' provides crustal and subcrustal cross sections of five major structural features.

A distance of 303 km marks the location of a bathymetric maximum to the south of the Cocos ridge. North of this location, the ridge rises to a minimum depth of 1.1 km and generates a maximum free-air anomaly of +38 mgal. The computed depth to the Mohorovicic discontinuity beneath this ridge is 19 km, 1 km deeper than the mapped depth.

At 500 km, the fracture zone at  $85^{\circ}20'W$  is expressed as a narrow trough in a broad topographic rise. The depth changes from 2.0 km on the north flank of this trough to 3.1 km at its center; the corresponding free-air anomaly changes from +22 mgal to -15 mgal. The trough asymmetrically splits a broad topographic rise from a depth of 2.8 km, at 44 km, to 3.5 km, at 611 km. The topographic rise is reflected in a deepening of the Mohorovicic discontinuity from 10.7 km, at 360 km, to 13.7 km beneath the fracture zone.

Between local bathymetric deeps of 3.5 km, at 695 km, and 3.1 km, at 1022 km, the Carnegie ridge rises to a depth of 1.05 km, exhibits a maximum free-air anomaly of +52 mgal, and reflects a

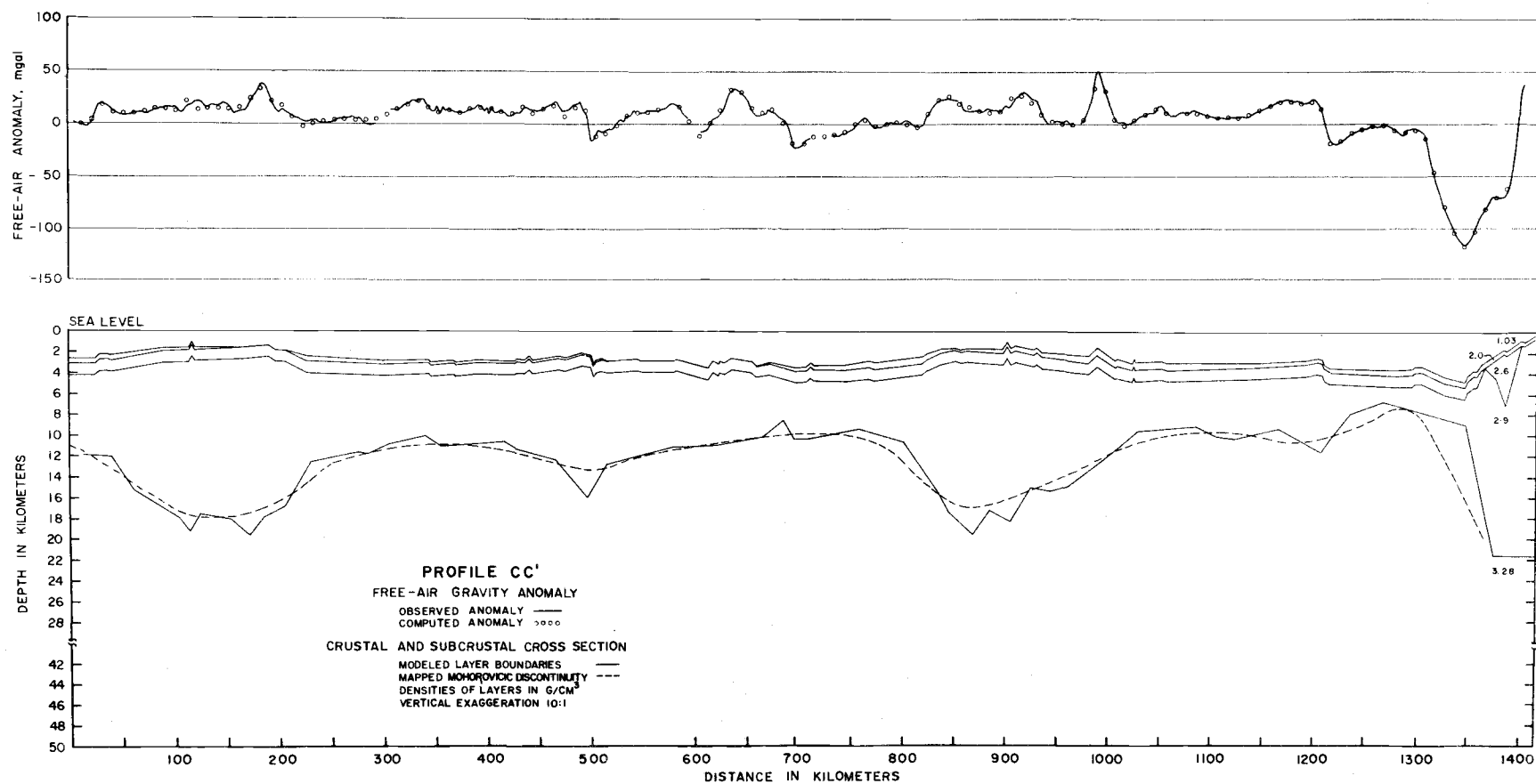


Figure 13. Crustal and subcrustal cross section for free-air gravity anomaly Profile CC'.

deepening of the Mohorovicic discontinuity to 18.5 km, 2 km deeper than the mapped depth.

From the 1022 km deep to a distance of 1210 km, the bottom rises to a depth of 2.6 km, the free-air anomaly increases from 0 mgal to +25 mgal, and the crust-mantle interface deepens 1 km from 9.5 km to 10.5 km. At 1210 km, a major discontinuity exists, which causes a 1 km vertical downdrop of the bottom to a depth of 3.6 km and an associated -45 mgal change in the free-air anomaly from +25 mgal to -20 mgal. To the south of this discontinuity, the bottom remains flat while the Mohorovicic discontinuity rises to 6.5 km, the shallowest depth to the crust-mantle interface on any of the 3 profiles. The 1210-km discontinuity, therefore, is the most profound structural discontinuity found anywhere in the survey area. It corresponds to a major northeast-trending fracture zone, as indicated by its trace on the filtered free-air anomaly map.

From a slight rise in the bottom to a depth of 3.3 km, at 1299 km, the depth increases to 4.8 km, and the free-air anomaly changes from -5 mgal to -118 mgal, at 1345 km, the axis of the Peru-Chile trench.

## MOHOROVICIC DISCONTINUITY MAP

### Computation of Depth to the Mohorovicic Discontinuity and Construction of Map

In a manner analogous to the computation of a simple bouguer anomaly, the depth to the Mohorovicic discontinuity was computed using the infinite-slab approximation.

Solution of the equations listed in Figure 7 for the depth to the Mohorovicic discontinuity yields the following result:

$$T = [A - BG + \sum_{i=1}^3 (R_i T_i) - R_4 (\sum_{i=1}^3 T_i)] / (R_5 - R_4)$$

where:  $A = R_5 D - AT/K$  and  $B = 1/K$ . This is the algorithm used to compute the depth to the Mohorovicic discontinuity via programs THICKOMP and FILTGRID (Appendix 1).

The process by which the basemap for contouring depth to the Mohorovicic discontinuity was constructed can most easily be discussed in reference to Figure 16.

The magnetic-tape file of gridded and averaged surface-ship geophysical data was reformatted, and data representing non-empty grid squares was punched on cards, to which the sediment thickness measured from the isopach map of van Andel et al. (1971a) was added manually. Program FILTHICK computed the depth to the Mohorovicic discontinuity at each grid point and then filtered these

depths using filtering phase 2 to operate on the D array that consisted of the computed depth to the Mohorovicic discontinuity and the N array that consisted of the number of free-air anomaly values in each grid square.

The pendulum station data were processed by manually adding sediment thickness to each record in the same manner as above. Program THICKOMP then computed the depth to the Mohorovicic discontinuity at each point.

Both of these files were then plotted on a mercator chart, which was later contoured by hand, ignoring as before all data from pendulum stations that were closer than 28 km (15 nm) to filtered data values.

### Discussion of Map

Figure 14 is the contoured map of the computed depth to the Mohorovicic discontinuity. Excluding the continental margin, the only features of this map overlying a crust-mantle interface deeper than 15 km are the four named aseismic ridges. Although the depth to the Mohorovicic discontinuity beneath the Coiba and Malpelo ridges is less than 16 km, that beneath the Cocos and Carnegie ridges is greater than 18 km. The apparent 3-km discrepancy in the depth to the crust-mantle interface between the two smaller and the two larger ridges is primarily an artifact of the infinite-slab approximation.

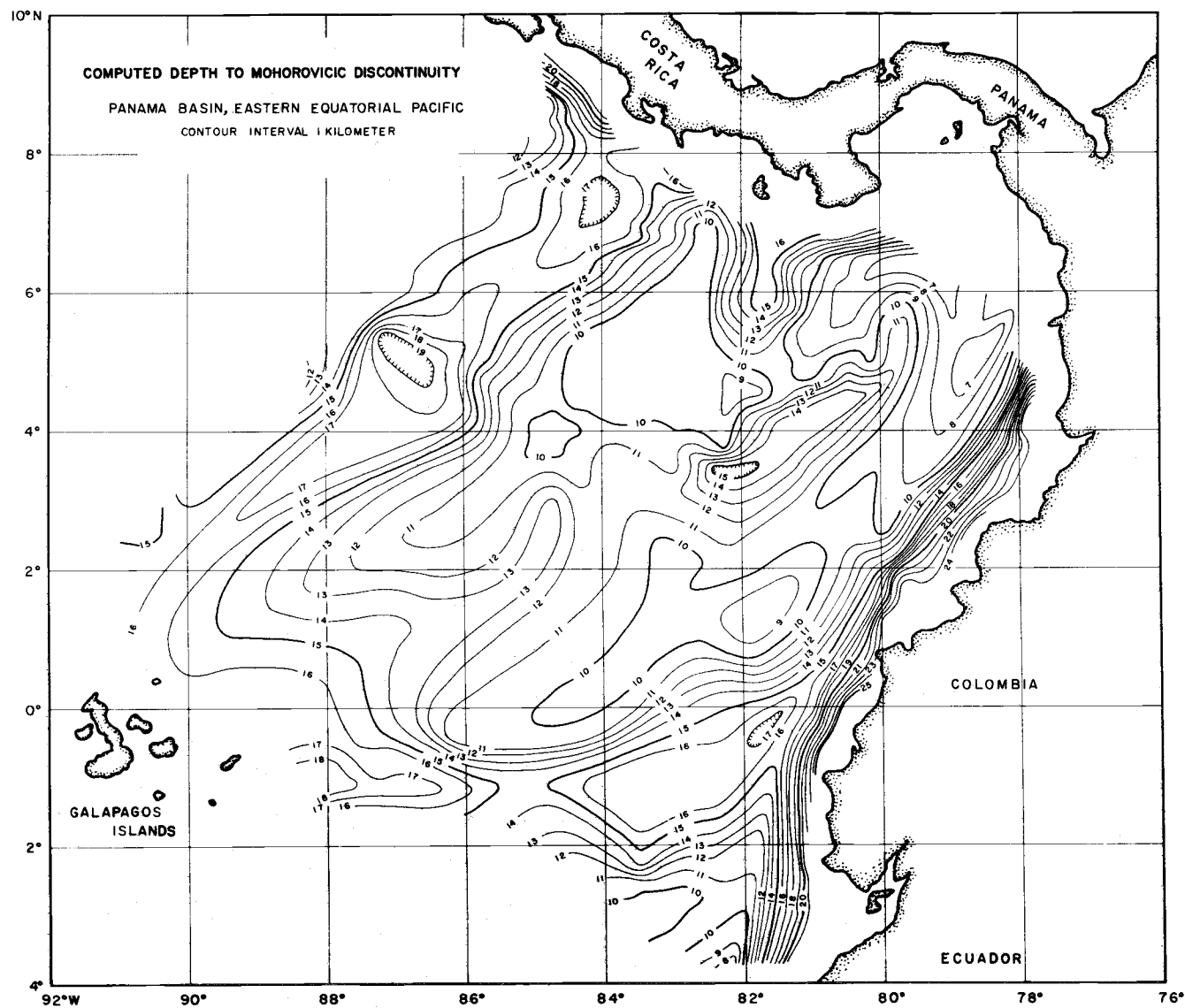


Figure 14. Map of the computed depth to the Mohorovicic discontinuity.

The effect of this approximation is quite evident on the crustal sections where the departure between the mapped and modeled Mohorovicic discontinuity is much more pronounced on the smaller ridges. The maximum depths to the crust-mantle interface beneath the Cocos and Carnegie ridges lie well seaward of their landward ends, giving the slight suggestion of landward shoaling in conformance with the observed increasing free-air anomalies. The eastern end of the Carnegie ridge is separated from the continental margin by a ridge in the Mohorovicic discontinuity, with a relief of over 1 km.

The depth to the Mohorovicic discontinuity is less than 9 km at four locations, each east of the Panama fracture zone. The first location, at  $3^{\circ}30'S$  latitude,  $82^{\circ}30'W$  longitude, corresponds to a band of abnormally thin crust between the major fracture zone at 1210 km on Profile CC' and the Peru-Chile trench. The second location corresponds to the deep region between the Malpelo and Carnegie ridges. The third location, at  $4^{\circ}30'N$  latitude,  $82^{\circ}W$  longitude, corresponds to the 3600 km deep between the Coiba and Malpelo ridges. The fourth location is an area, much larger than the other three, representing the deep region surrounding the abnormally shallow structures of the eastern basin and the area north of  $3^{\circ}N$  latitude in which the free-air anomaly is predominantly greater than +20 mgal.

South and east of the Malpelo ridge, two of the shallow areas mentioned above are separated by a trough at about  $80^{\circ}30'W$  longitude.



This trough and the associated inflections on the 10 km to 13 km contours are the expressions of the Yaquina graben.

The Mohorovicic discontinuity underlying the western basin is characterized by its smoothness and the fact that there are no places where it is shallower than 9 km or deeper than 15 km. The sinuous trough running from where the 14-km contour takes a sharp bend at  $1^{\circ}\text{N}$  latitude,  $87^{\circ}\text{W}$  longitude to the western termination of the Malpelo ridge against the Panama fracture zone, corresponds to the Galapagos spreading center and the various transform faults that connect its broken segments. As in the case of the bathymetric ridge, where this feature is crossed by Profile CC', it corresponds to the fracture zone at  $85^{\circ}20'\text{W}$  longitude.

## SYNTHESIS AND CONCLUSIONS

The aseismic ridges, in addition to being the most obvious structural features in the Panama Basin, are important in that a knowledge of their structure is critical to an understanding of the regional tectonic history. The results of van Andel et al. (1971a) and leg 16 of the deep sea drilling project indicate a similarity of the shallow structure of these ridges; a similarity in their deep structure is suggested by the fact that their crustal thicknesses are identical, within the accuracy of the computations. What their structure actually is in cross section and how it changes along the trend of these ridges is difficult to determine with the available data.

Figure 15 presents three possible structural cross sections of the portion of Profile CC' (Figure 13) that spans the Carnegie ridge. These sections account for the observed depth and free-air anomaly by partial isostatic adjustment to thickening of layer 2, thickening of layer 3, and emplacement of low-density upper mantle. In Figure 15a, a 5-km thickening of layer 2 results in a depth to the Mohorovicic discontinuity of 13 km. The scale at the top of this figure corresponds to the scale of Figure 13. In Figure 15b, a 17-km depth to the crust-mantle interface is caused by a 9-km thickening of layer 3. In Figure 15c, a 14.5-km-thick lense of low-density upper-mantle material results in a Mohorovicic discontinuity depth of 8 km or a

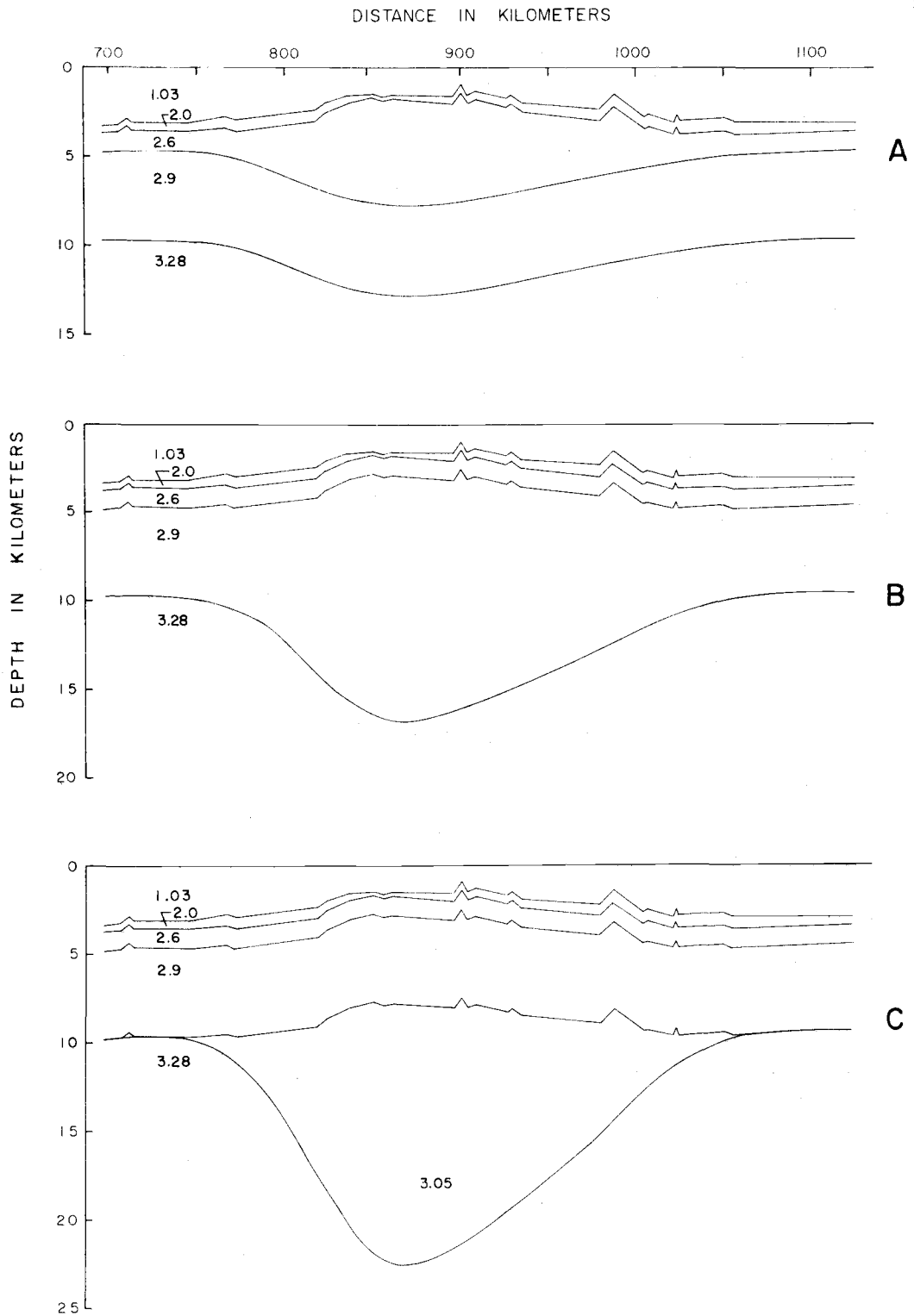


Figure 15. Alternative crustal sections for the Carnegie Ridge. (a) Thickening of Transition Layer, (b) Thickening of Oceanic Layer, and (c) Emplacement of Low-Density Upper Mantle.

depth of 22.5 km to the interface between the low-density mantle and the normal mantle below.

Deciding among these models is a difficult if not impossible task, based on the existing information. The model depicting a purely extrusive origin for the ridges (Figure 15a) is highly unlikely in light of the blocky, horst-like appearance of the ridges and the fact that known volcanic ridges are partially extrusive, exhibiting a thickening of both layers 2 and 3. However, because of the proximity of these ridges to the Galapagos Islands and their suggested origin at the Galapagos hot spot, it seems probable that they are at least partially volcanic. Therefore, the remaining two models are also unlikely, although both are supported by existing models.

The model invoking a purely intrusive origin (Figure 15b) is in agreement with a north-south crustal section across the Hawaiian archipelago (Dehlinger, 1969, Figure 9). This section uses a thickening layer 3 to produce a Mohorovicic discontinuity depth of 17.5 km, surprisingly close to the 17-km depth of Figure 15b. However, across the Hawaiian ridge Dehlinger's section is not constrained by seismic refraction control; therefore, it is no more reliable than the section in Figure 15b.

The model employing a lense of low density upper mantle (Figure 15c) is in close agreement with the crustal section of Bowin (1973, Figure 7) across the Ninety East ridge, at 4°N latitude. The

problem with this comparison is that the Ninety East ridge is clearly not volcanic, whereas the Cocos and Carnegie ridges probably are. Furthermore, the Ninety East ridge does not line up with the proposed absolute plate motion, although the Cocos and Carnegie ridges do.

The structure of the aseismic ridges is probably a combination of the above three models, but what the exact combination is remains to be answered. The Hawaiian ridge sections of Shor (1960), Shor and Pollard (1964), Furumoto et al. (1968), and Malahoff and Woollard (1970) show a thickening of both layers 2 and 3, but the Hawaiian ridge is clearly depositional and smooth in profile as opposed to the blocky, fault-controlled shape of the Carnegie and Cocos ridges. The Bowers ridge (Ludwig et al., 1971) is formed by a combined thickening of both crustal layers and the emplacement of a lense of low-density upper mantle, but its similarity with the Cocos and Carnegie ridges is highly suspect. In short, there is no published model that satisfactorily accounts for all of the characteristics of these ridges.

The free-air anomaly associated with the Cocos and Carnegie ridges varies from near zero close to the Galapagos pedestal to greater than +40 mgal at their landward ends. Therefore, there must be some mechanism acting to force the landward ends out of isostatic equilibrium. Because both of these ridges appear to

terminate active trenches, the most likely mechanism to accomplish this is local uplift caused by bending of the lithosphere in response to subduction at the trenches. The bathymetry does not indicate shoaling, although it is difficult to differentiate between depositional and tectonic features. In spite of this difficulty, the computed depth to the Mohorovicic discontinuity does suggest a shoaling mantle beneath these ridges.

With the exception of the aseismic ridges, perhaps the most striking feature of the Panama basin is the large block bounded on the north and east by the continental margin, on the west by the Panama fracture zone, and on the south by  $3^{\circ}\text{N}$  latitude. Containing the Coiba and Malpelo ridges, this block is characterized by its great relief, its predominantly positive free-air gravity anomalies, and its abnormally shallow depth to the Mohorovicic discontinuity.

Although the depth of the Coiba and Malpelo ridges is less than 1200 m, the depth of the surrounding area is predominantly greater than 3000 m, reaching a maximum depth of 3600 m at the deepest points in the entire survey area. Similarly, although the depth to the Mohorovicic discontinuity is greater than 15 km beneath the aseismic ridges, it is less than 8 km in the surrounding area and, in fact, reaches a minimum of less than 7 km. In the survey area there are no other locations at which the depth to the crust-mantle

interface is less than 7 km, only one other location outside the Panama Basin at which it is less than 8 km, and only two other locations at which it is less than 9 km. It is, therefore, fair to conclude that the Mohorovicic discontinuity beneath this block is anomalously shallow or, alternatively, that the upper mantle has an anomalously high density. Neither of these conclusions are consistent with a young crust.

The filtered free-air gravity anomaly map provides the most striking evidence for an east-west discontinuity at  $3^{\circ}\text{N}$  latitude. North of this latitude, although there is a local minimum of less than -20 mgal, the free-air gravity anomalies are predominantly greater than +20 mgal. In fact, the greater than +60-mgal anomaly associated with the Coiba ridge is the highest free-air anomaly in the survey area.

These observations suggest that north of  $3^{\circ}\text{N}$  latitude the crust is held out of isostatic equilibrium in an anomalously high position. South of  $3^{\circ}\text{N}$  latitude, however, the crust is near isostatic equilibrium as indicated by moderate free-air gravity anomalies ranging only from -10 mgal to +20 mgal. Furthermore, whereas the northern half of the eastern basin is characterized by its ruggedness, the southern half is characterized by its smoothness.

The southern half of the basin is predominantly deeper than 3000 m, and it is underlain by a Mohorovicic discontinuity that

reaches a minimum depth of less than 9 km. The only irregularity in this otherwise monotonously smooth basin is the Yaquina graben, which results in a slight shoaling of the computed Mohorovicic discontinuity.

The western basin is also characterized by its smoothness and moderate free-air gravity anomalies. The spreading centers and fracture zones contained therein are for the most part characterized by a lack of gravitational signature, a shoaling of the bottom, and an apparent deepening of the Mohorovicic discontinuity, most probably the reflection of underlying prisms of low-density upper mantle. The only exception to the above generalization is the northern end of the Panama fracture zone between the Cocos and Coiba ridges. Here, the fracture zone is expressed as a graben under which the Mohorovicic discontinuity apparently shoals. An explanation for this radical departure from normal is that the true character of the fracture zone is simply masked by the adjacent ridges, and the graben-like bathymetry is the result of differential uplift in response to lithospheric subduction. The two aseismic ridges are uplifted higher than the intervening crust because they are thicker and more difficult to bend. This explanation is supported by the fact that the magnitude and width of the positive free-air anomalies seaward of the subduction zone is much greater for the ridges than it is for the intervening crust.



The fracture zone at  $85^{\circ}20'W$  longitude appears to divide the western basin into two distinct provinces. East of this fracture zone, the basin is characterized by depths greater than 3000 m conforming to the normal age-depth relation of Sclater et al. (1971) and apparent mantle depths ranging from greater than 11 km at the Costa Rica rift zone to less than 10 km on its far flanks. West of this fracture zone, however, the basin is abnormally shallow and overlies an abnormally deep Mohorovicic discontinuity. Although the abnormal depths of this western province can be explained by crustal thickening caused by the proximity of the Cocos and Carnegie ridges, the reason for the sharp discontinuity at  $85^{\circ}20'W$  longitude is unclear, as is the relationship between it and the saddles in the Cocos and Carnegie ridges, both of which also line up with the fracture zone at  $85^{\circ}20'W$  longitude.

No existing theory satisfactorily explains all of the geological and geophysical observations made in the Panama Basin and its surroundings. However, most of the gross structural features discussed above can be explained, using the plate tectonic model of Minster et al. (In press), by the relative motion of the Cocos, Nazca, North American, and South American lithospheric plates and their absolute motion with respect to the Galapagos hot spot.

In the context of this model, the Cocos and Carnegie ridges are formed by the trajectory of the Cocos and Nazca plates over the

Galapagos hot spot. The observed free-air gravity anomalies dictate that the ridges are compensated soon (less than 1 m. y.) after formation, but forced out of isostatic equilibrium as they progress toward their respective trenches by upbending in response to subduction.

The observed structure and tectonics of the western basin is the direct result of north-south relative motion between the Cocos and Nazca lithospheric plates and the northeast-southwest relative motion between the Cocos and North American plates. Presumably, in the past, these same relative plate motions were active in the eastern basin. However, because the north-south component of the relative motion between the Nazca and South American plates is small, the Cocos-Nazca spreading center migrated northward at half its spreading rate until, at some undetermined date, it was subducted at the eastward extension of the present Middle America trench, thereby forming a stable triple junction (McKenzie and Morgan, 1969) between the Cocos, Nazca, and North American plates. The history and geometry of this triple junction is analogous to the triple junction at the eastern end of the Mendocino fracture zone between the Farralon, Pacific, and North American plates (McKenzie and Morgan, 1969). Based on the apparent anomalously thin crust in the eastern basin, it seems likely that the formation of this triple junction is not a recent event.

The present structure and tectonics of the eastern basin are, therefore, largely the result of the east-west relative motions between the Nazca plate and the two continental plates to the north and west. Because the model of Minster et al. (In press) predicts that in the Panama Basin the Nazca plate is moving approximately  $N80^{\circ}E$  at a rate of 8.4 cm/year relative to the South American plate, subduction is occurring at the continental margin of South America. Furthermore, since the relative motion between the North American and South American plates is small, the relative motion between the Nazca and North American plates must be accommodated by a left-lateral fracture zone near the continental margin south of Panama.

The world seismicity map supports these conclusions about the nature of the relative motion between the Nazca plate and the adjacent continental plates. The presence of intermediate-focus earthquakes under the South American continent indicates that subduction is occurring at this margin. The reason for the comparatively low number of these earthquakes, between the equator and  $4^{\circ}N$  latitude, is the slower convergence rate resulting from the lower angle ( $40^{\circ}$ ) between the direction of relative motion and the continental margin. In fact, the component of relative motion parallel to this margin is greater than the convergence rate, suggesting a possible cause for at least some of the right-lateral shear apparent on the Guayaquil-Dolores megashears (Case et al., 1971) and the northeast-trending fractures

in sea floor (van Andel et al., 1971a). The presence of shallow-focus earthquakes and the relative absence of intermediate-focus earthquakes along the continental margin south of Panama is consistent with the proposed strike-slip motion between the Nazca and North American plates.

Unfortunately, there are no published focal mechanisms for the earthquake epicenters associated with the boundary of the North American plate. However, the two focal mechanisms of Molnar and Sykes (1969) along the boundary of the South American plate are consistent with underthrusting.

As shown by Frank (1968), the only way a spherical shell can be bent inward without changing its surface area is by reversal of curvature, thereby resulting in a spherical depression whose trace on the spherical shell is a small circle. This and the world-wide preponderance of convex subduction zones suggest a possible explanation for the striking discontinuity at  $3^{\circ}\text{N}$  latitude in the structure of the eastern basin. South of  $3^{\circ}\text{N}$  latitude the continental margin is convex. Therefore, the Nazca plate is subducted with little or no secondary deformation, causing its bottom to be smooth and its associated free-air anomaly to be moderate. North of  $3^{\circ}\text{N}$  latitude, however, the continental margin is sharply concave, forcing the subducting lithosphere into a situation in which its surface area cannot be conserved. Therefore, the crust is subjected to a great

deal of compression and uplift prior to subduction, and after subduction it is subjected to tension. The presubduction compression and uplift could be great enough to account for the observed relief and lack of isostatic equilibrium in the northern half of the eastern basin. Similarly, the apparent east-west discontinuity at  $6^{\circ}\text{N}$  latitude in the epicenters of the intermediate-focus earthquakes is caused by a tension-induced tear in the subducted plate.

Although the above model for the structure and tectonics of the Panama Basin provides a plausible explanation for most of the major features, it does not explain the existence of the Yaquina graben or the apparent similarity in the sediment cover, relief, and age of the aseismic ridges. A detailed investigation of the magnetic anomalies in the eastern basin and a seismic refraction survey of the aseismic ridges would go a long way toward resolving these observations.

## BIBLIOGRAPHY

- Anderson, D. L. 1967. Latest information from seismic observations. In: T. F. Gaskell (editor), *The Earth's Mantle*. New York, Academic Press. pp. 355-420.
- Archambeau, C. B., E. A. Flinn and D. G. Lambert. 1969. Fine structure of the upper mantle. *Journal of Geophysical Research* 74:5825-5866.
- Barday, R. J. 1971. Free-air gravity anomalies south of Panama and Costa Rica. NOAA Technical Memorandum ERL AOML-14. 51 p.
- Bowin, C. 1973. Origin of the ninety east ridge from studies near the equator. *Journal of Geophysical Research* 78:6029-6043.
- Bruins, G. J., R. Dorrestein, H. J. A. Vasseut, G. Bakker and L. Otto. 1960. Atlantic, Caribbean and Pacific cruises. In: *Gravity Expeditions 1948-1958*, v. 5, Rijkscommissie Voor Geodesie, Delft, Netherlands. 117 p.
- Case, J. E., L. G. Duran S., Alfonso Lopes R. and W. R. Moore. 1971. Tectonic investigations in western Columbia and eastern Panama. *Geological Society of America Bulletin* 82:2685-2712.
- Clark, S. P., Jr. and A. E. Ringwood. 1964. Density distribution and constitution of the mantle. *Reviews of Geophysics* 2:35-88.
- Couch, R. W. 1969. Gravity and structures of the crust and subcrust in the northeast Pacific ocean west of Washington and British Columbia. Ph.D. Thesis. Corvallis, Oregon State University, 179 p.
- Dehlinger, P. 1969. Gravity and its relation to topography and geology in the Pacific ocean. In: P. J. Hart (editor), *The Earth's Crust and Upper Mantle*. Geophysical Monograph 13, American Geophysical Union, Washington, D. C., pp. 352-363.
- Ewing, J. and M. Ewing. 1959. Seismic refraction measurements in the Atlantic Ocean basins, in the Mediterranean Sea, on the mid-Atlantic ridge, and in the Norwegian Sea. *Geological Society of America Bulletin* 70:291-318.

- Forsyth, D. W. and F. Press. 1971. Geophysical tests of petrological models of the spreading lithosphere. *Journal of Geophysical Research* 76:7963-7979.
- Frank, F. C. 1968. Curvature of island arcs. *Nature* 220:363.
- Furumoto, A. S., G. P. Woollard, F. Campbell and D. Hussong. 1968. Variations in the thickness of the crust in the Hawaiian Archipelago. In: L. Knopoff, C. L. Drake and P. J. Hart (editors), *The Crust and Upper Mantle of the Pacific Area*. Monograph 12, American Geophysical Union, Washington, pp. 94-111.
- Gemperle, M. and K. Keeling. 1970. Geophysical data reduction and plotting computer programs. Technical Report No. 180. Reference 70-10, Department of Oceanography, Oregon State University. 56 p.
- Gemperle, M., K. Keeling and G. Watson. 1974. Geophysical data reduction and plotting computer programs. Technical Report, Department of Oceanography, Oregon State University. (In preparation).
- Goslin, J., P. Beuzart, J. Francheteau and X. LePichon. 1972. Thickening of the oceanic layer in the Pacific ocean. *Marine Geophysical Researches* 1:418-427.
- Green, R. W. E. and A. L. Hales. 1968. The travel times of P waves to  $30^{\circ}$  in the Central United States and upper mantle structures. *Bulletin of the Seismological Society of America* 58:267-290.
- Grim, P. J. 1970a. Connection of the Panama fracture zone with the Galapagos rift zone, Eastern Tropical Pacific. *Marine Geophysical Researches* 1:85-90.
- \_\_\_\_\_. 1970b. Bathymetric and magnetic anomaly profiles from a survey south of Panama and Costa Rica. ESSA Technical Memorandum ERLTM-AOML 9. 87 p.
- Hayes, D. E. 1966. A geophysical investigation of the Peru-Chile trench. *Marine Geology* 4:309-351.

- Heirtzler, J. R., G. O. Dickson, E. M. Herron, W. C. Pitman, III and X. Le Pichon. 1968. Marine magnetic anomalies, geomagnetic field reversals, and motions of the ocean floor and continents. *Journal of Geophysical Research* 73:2119-2136.
- Heiskanen, W. A. 1938. Catalogue of the isostatically reduced gravity stations. Helsinki. 139 p. (International Association of Geodesy. Isostatic Institute. Publication no. 5).
- Herron, E. M. and J. R. Heirtzler. 1967. Sea-floor spreading near the Galapagos. *Science* 158:775.
- Herron, E. M. 1972. Sea-floor spreading and the cenozoic history of the east-central Pacific. *Geological Society of America Bulletin* 83:1671-1692.
- Hey, R. N., K. S. Deffeyes, G. L. Johnson and A. Lowrie. 1972. The Galapagos triple junction and plate motions in the East Pacific. *Nature* 237:20.
- Holden, J. C. and R. S. Dietz. 1972. Galapagos gore, NazCoPac triple junction and Carnegie/Cocos ridges. *Nature* 235:266-269.
- Johnson, L. R. 1967. Array measurements of P velocities in the upper mantle. *Journal of Geophysical Research* 72:6309-6325.
- Johnson, G. L. and A. Lowrie. 1972. Cocos and Galapagos ridges: result of the Galapagos "hot spot?". *Earth and Planetary Science Letters* 14:279-280.
- Lewis, B. T. R. and R. P. Meyer. 1968. A seismic investigation of the upper mantle structure to the west of Lake Superior. *Bulletin of the Seismological Society of America* 58:565-596.
- Lewis, B. T. R. and L. M. Dorman. 1970. Experimental isostasy 2. an isostatic model for the U. S. A. derived from gravity and topographic data. *Journal of Geophysical Research* 75: 3367-3386.
- LePichon, X., R. E. Houtz, C. L. Drake and J. E. Nafe. 1965. Crustal structure of the mid-ocean ridges 1. Seismic refraction measurements. *Journal of Geophysical Research* 70:319-339.



- Ludwig, W. J., J. E. Nafe and C. L. Drake. 1970. Seismic refraction. In: A. E. Maxwell (editor), *The Sea*, Vol. 4, Part I. New York, Wiley-Interscience. pp. 53-84.
- Ludwig, W. J., S. Murauchi, N. Den, M. Ewing, H. Hotta, R. E. Houtz, T. Yoshii, T. Asanuma, K. Hagiwara, T. Sato and S. Ando. 1971. Structure of Bowers ridge, Bearing Sea. *Journal of Geophysical Research* 76:6350-6366.
- Malahoff, A. and G. P. Woollard. 1970. Geophysical studies of the Hawaiian Ridge and the Murray fracture zone. In: A. E. Maxwell (editor), *The Sea*, Vol. 4. Part II. New York, Wiley-Interscience, pp. 73-131.
- McKenzie, D. P. and W. J. Morgan. 1969. The evolution of triple junctions. *Nature* 224:125-133.
- Menard, H. W. and T. Atwater. 1969. Origin of fracture zone topography. *Nature* 222:1037-1040.
- Minster, J. B., T. H. Jordan, P. Molnar and E. Haines. 1974. Numerical modeling of instantaneous plate tectonics. Contribution No. 2274, Division of Geology and Planetary Sciences, California Institute of Technology, Pasadena, California. (In press).
- Molnar, P. and L. R. Sykes. 1969. Tectonics of the Caribbean and Middle America regions from focal mechanisms and seismicity. *Geological Society of America Bulletin* 80:1639-1684.
- Pitman, W. C., III, E. M. Herron and J. R. Heirtzler. 1968. Magnetic anomalies in the Pacific and sea floor spreading. *Journal of Geophysical Research* 73:2069-2085.
- Raff, A. 1968. Sea-floor spreading--another rift. *Journal of Geophysical Research* 73:3699.
- Raitt, R. W. 1956. Seismic refraction studies of the Pacific ocean basin, 1, Crustal thickness of the central equatorial Pacific. *Geological Society of America Bulletin* 67:1623-1640.
- Sclater, J. G., R. N. Anderson and M. L. Bell. 1971. Elevation of ridges and evolution of the central eastern Pacific. *Journal of Geophysical Research* 76:7888-7915.

- Sclater, J. G. and K. D. Klitgord. 1973. A detailed heat flow, topographic, and magnetic survey across the Galapagos spreading center at 86°W. *Journal of Geophysical Research* 78:6951-6975.
- Shor, G. G. 1960. Crustal structure of the Hawaiian Ridge near Gardner Pinnacles. *Bulletin of the Seismological Society of America*. 50:563-573.
- Shor, G. G. and D. D. Pollard. 1964. Mohole site selection north of Maui. *Journal of Geophysical Research*. 69:1627-1637.
- Shor, G. G., Jr., H. W. Menard and R. W. Raitt. 1970. Structure of the Pacific Basin. In: A. E. Maxwell (editor), *The Sea*, Vol. 4, Part II. New York, Wiley-Interscience, pp. 321-358.
- Talwani, M., J. L. Worzel and M. Landisman. 1959a. Rapid computations for two-dimensional bodies with application to the Mendocino submarine fracture zone. *Journal of Geophysical Research* 64:49-59.
- Talwani, M., G. H. Sutton and J. L. Worzel. 1959b. A crustal section across the Puerto Rico Trench. *Journal of Geophysical Research* 64:1545-1555.
- Talwani, M. 1964. A review of marine geophysics. *Marine Geology* 2:29-80.
- Talwani, M., X. LePichon and M. Ewing. 1965. Crustal structure of the mid-ocean ridges 2. computed model from gravity and seismic-refraction data. *Journal of Geophysical Research* 70:341-352.
- van Andel, Tj. H., G. R. Heath, B. T. Malfait, D. F. Heinrichs and J. I. Ewing. 1971a. Tectonics of the Panama Basin, Eastern Equatorial Pacific. *Geological Society of America Bulletin* 82:1489-1508.
- van Andel, Tj. H., R. P. von Herzen and J. D. Phillips. 1971b. The Vema fracture zone and the tectonics of transverse shear zones in the oceanic crustal plates. *Marine Geophysical Researches* 1:261-283.

Vening Meinesz, F. A. 1948. Gravity expeditions at sea 1923-1938, Vol. 4, Publ. Neth. Geod. Comm., Delftche Vitgevers Mij, Delf, 1948.

Worzel, J. L. and G. L. Shurbet. 1955. Gravity interpretations from standard oceanic and continental crustal sections. Geological Society of America Special Paper 62:87-100.

Worzel, J. L. 1965. Pendulum gravity measurements at sea 1936-1959. New York, John Wiley and Sons, Inc. 422 p.




## APPENDICES

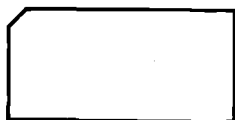
## APPENDIX I

## DATA FLOW AND COMPUTER PROGRAM DOCUMENTATION

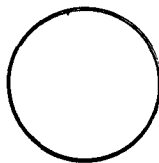
Included here is a diagram illustrating the flow of data (Figure 16), a discussion of the individual data files and listings, and a documentation and listing of the computer programs.

In the data flow diagram, the following notation is used:

-  Step in data flow that is executed only once.
-  Step in data flow that is executed twice: once for bathymetry, and once for free-air gravity anomaly.
-  Step in data flow that is executed three times: once for free-air gravity anomaly, once for magnetic anomaly, and once for bathymetry.



BCD card-image file.



Binary file.

Both of the binary files are stored on magnetic tape, and the tape numbers are given in parentheses. In all files except BFILE 1, free-air gravity anomaly is expressed in tenths of milligals, depth and thicknesses are expressed in meters, and latitude and longitude are expressed in degrees and minutes, according to the unconventional left-handed coordinate system in which north and west are positive.

# DATA FLOW

75

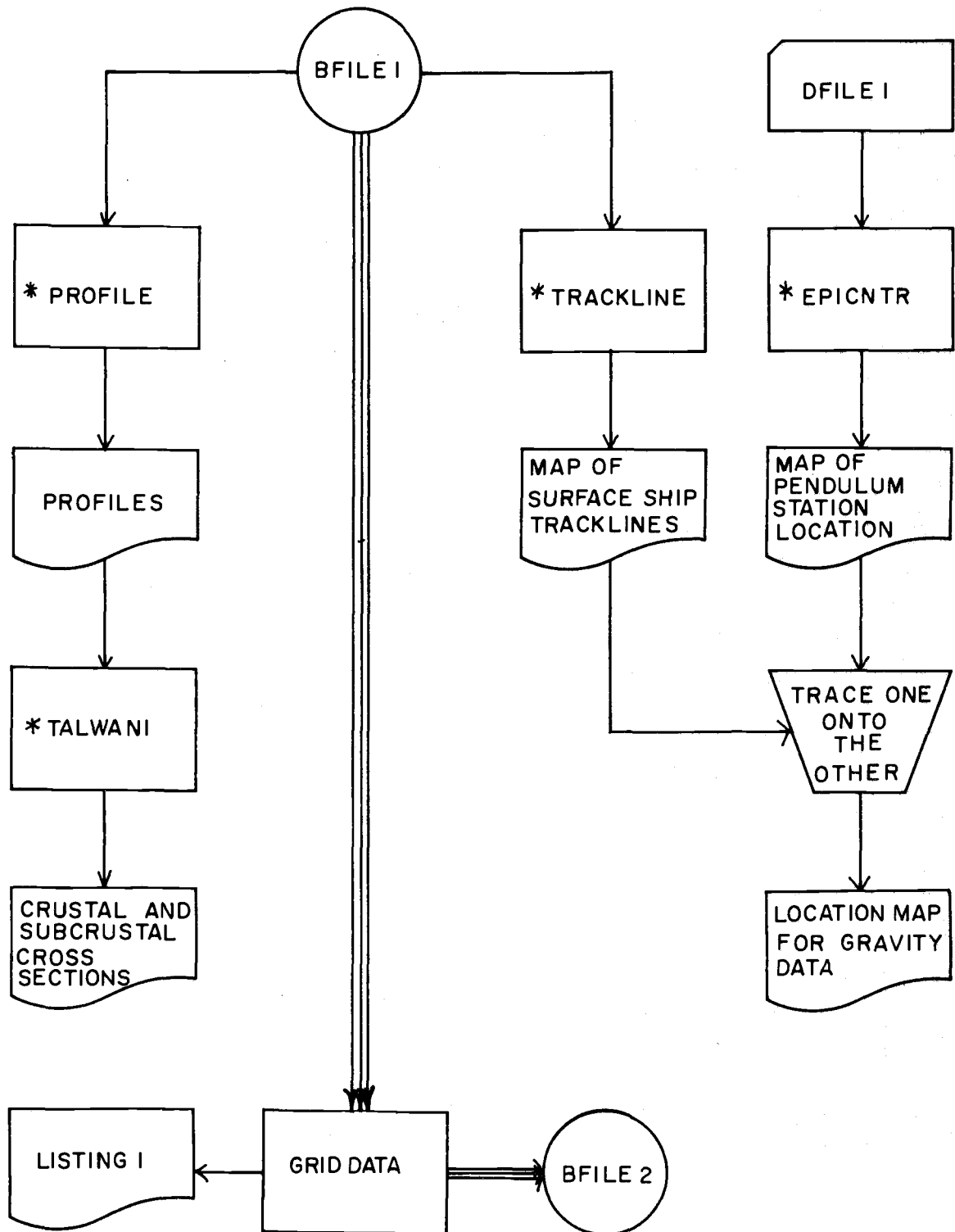


Figure 16. Diagram illustrating the flow of data.

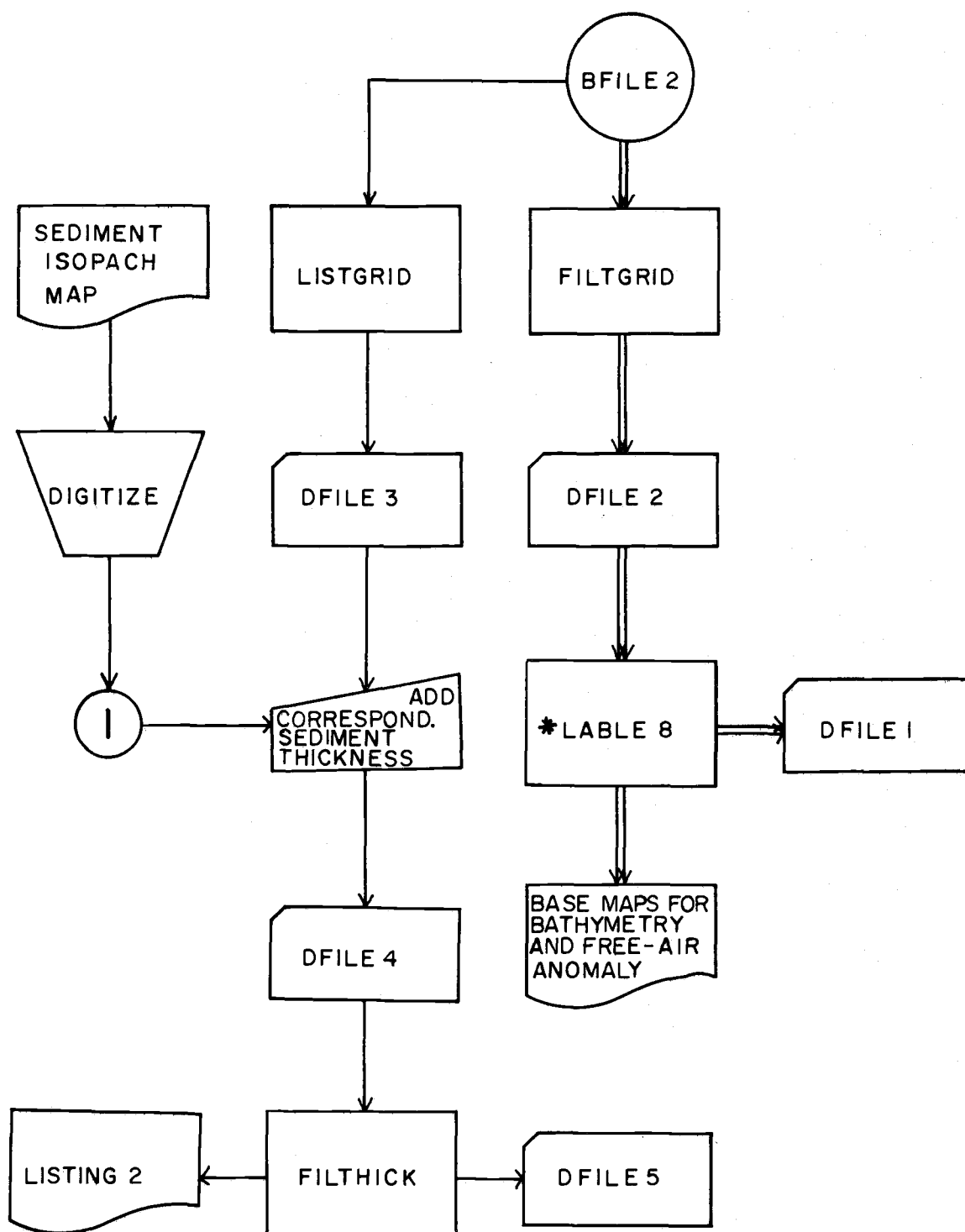


Figure 16. Continued.

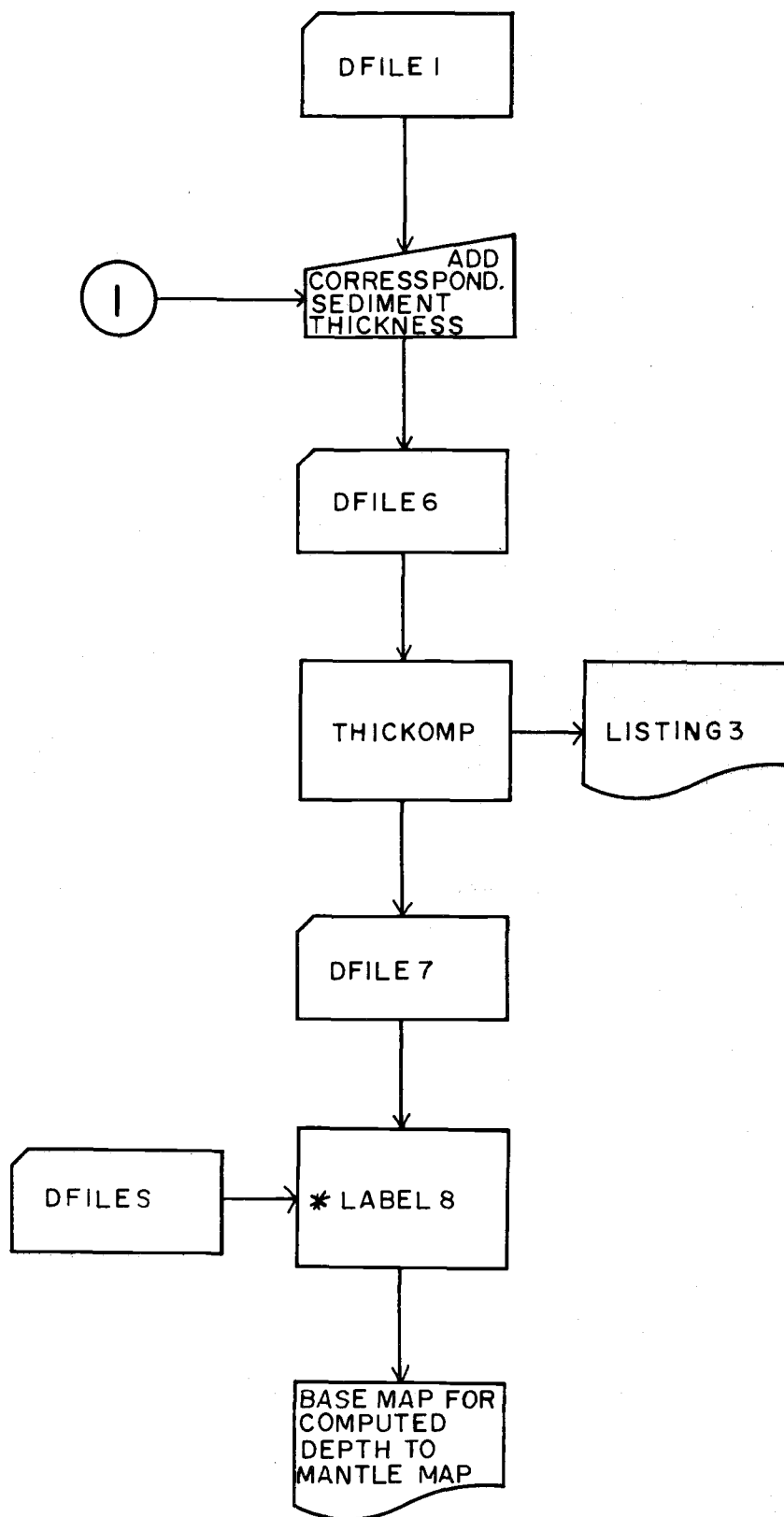


Figure 16. Continued.



The starred programs shown on the flow diagram are:

\*PROFILE: Profiles input data.

\*TRACKLINE: Plots tracklines on a mercator chart.

Both of the above programs accept data in NGDC binary format. The programs and format are documented by Gemperle et al. (In prep.).

\*EPICNTR: Plots the location of single points on a mercator chart.

\*LABEL8: Plots the location as well as the value of single data points on a mercator chart.

Both of the above programs accept data in BCD card-image form. The former is documented by Gemperle and Keeling (1970), and the latter, by Gemperle et al. (In prep.).

\*TALWANI: Computes gravitational attraction of a two-dimensional model. The program is documented by Couch (1969), but the technique on which the program is based is described by Talwani, et al. (1959).

All other programs and subroutines are documented and listed herein.

For each of these programs, the input file is on logical unit 1, the output file is on logical unit 2, and the listing, if any, is made on logical unit 10.

### Data Files and Listings

- BFILE1: (MT9105), Surface-ship geophysical data in NGDC binary format. In this format the unit of latitude and longitude is the decimal degree divided by  $10^4$ , and the sign convention is north and east positive.
- BFILE2: (MT9902), Gridded free-air gravity anomaly, magnetic anomaly, and bathymetry. Each of these three types of data is represented by 64 by 56 N and D arrays computed from a 15' by 15' grid.
- DFILE1: Pendulum station data. Filed in format (2(I5, F5.1), 2(6X, F6.0)), each record consists of latitude, longitude, free-air gravity anomaly, and depth.
- DFILE2: Filtered data (bathymetry or free-air gravity anomaly). Filed in format (2(I5, F5.1), F8.0), each record consists of latitude, longitude, and filtered value.
- DFILE3: Gridded free-air gravity anomaly and bathymetry data. Filed in format (2I10, I4, F8.0, 4X, F8.0) and representing one grid square in which there is at least one value of both free-air anomaly and depth, each record consists of J index, K index, number of free-air anomaly values, average free-air gravity anomaly, and average depth.
- DFILE4: Same as DFILE3 with sediment thickness appended to each record. The format for this file is (2I10, I4, F8.0, 4X, F8.0, F7.0).
- DFILE5: Filtered depth to mantle. Each record consists of latitude, longitude, and filtered depth to mantle filed in format (2(I5, F5.1), F8.0).
- DFILE6: Same as DFILE1 with sediment thickness appended to each record. The format for this file is (2(I5, F5.1), 2(6X, F6.0), 3X, F4.0).
- DFILE7: Depth to mantle computed from pendulum data. Each record consists of latitude, longitude, and depth to mantle filed in format (2(I5, F5.1), F8.0).

- LISTING1: Multi-paged listing of N and D arrays followed by the average, standard deviation, minimum, and maximum of the input data values.
- LISTING2: Listing of depths and thicknesses computed from gridded data. Listed in format (2I10, I4, 7F8.0) and representing one grid square, each record consists of J index, K index, number of free-air gravity anomaly values, average free-air gravity anomaly, average depth, sediment thickness, transition layer thickness, oceanic layer thickness, crustal thickness, and depth to mantle.
- LISTING3: Listing of depths and thicknesses computed from pendulum data. Listed in format (2(I5, F5.1), 4X, 7F8.0), each record consists of latitude, longitude, free-air gravity anomaly, depth, sediment thickness, transition layer thickness, oceanic layer thickness, crustal thickness, and depth to mantle.

```

SUBROUTINE FILTDATA
*****
C FROM TWO MATRICES REPRESENTING THE NUMBER OF VALUES AND
C THE AVERAGE VALUE IN EACH SQUARE OF A SIMPLE GRID,
C SUBROUTINE FILTDATA COMPUTES AND OUTPUTS THE
C FOLLOWING PARAMETERS: LATITUDE, LONGITUDE, AND
C FILTERED DATA VALUE. THE FILTERED VALUES ARE DETERMINED
C BY AVERAGING ALL VALUES IN EACH COMPOUND SQUARE MADE UP
C OF 4 ADJACENT SIMPLE GRID SQUARES, AND THE CORRESPONDING
C GEOGRAPHIC POSITIONS ARE ASSIGNED ACCORDING TO THE
C FOLLOWING CASES:
C *****
COMMON N(64,56),J(64,56)
1000 FORMAT (2(I5,F5.1),F8.0)
DO 100 J=1,63
DO 100 K=1,55
IF(N(J,K+1).NE.0.AND.N(J+1,K).NE.0) GO TO 10
IF(N(J,K).EQ.0) GO TO 100
IF(N(J+1,K+1).EQ.0) GO TO 20
C *****
C CASE 1 -- AT LEAST TWO DIAGONALLY OPPOSED SIMPLE GRID
C SQUARES ARE NON-EMPTY. IN THIS CASE THE
C ASSIGNED POSITION IS THE CENTER OF THE
C COMPOUND SQUARE.
C *****
10 SD=D(J,K)*N(J,K)+D(J+1,K+1)*N(J+1,K+1)
SD=SD+D(J+1,K)*N(J+1,K)+D(J,K+1)*N(J,K+1)
SN=N(J,K)+N(J+1,K+1)+N(J,K+1)+N(J+1,K)
TLONG=92.-J*0.25
TLAT=-4.+K*0.25
C *****
GO TO 60
20 IF(N(J,K+1).EQ.0) GO TO 40
IF(J.EQ.1) GO TO 30
IF(N(J-1,K).NE.0.OR.N(J-1,K+1).NE.0) GO TO 100
C *****
C CASE 2 -- GRID SQUARES J,K AND J,K+1 ARE NON-EMPTY, BUT
C J-1,K AND J-1,K+1 ARE EMPTY. IN THIS CASE THE
C ASSIGNED POSITION IS THE POINT MIDWAY BETWEEN
C THE CENTERS OF THE TWO NON-EMPTY SQUARES.
C *****
30 SD=D(J,K)*N(J,K)+D(J,K+1)*N(J,K+1)
SN=N(J,K)+N(J,K+1)
TLONG=92.-J*0.25+0.125
TLAT=-4.+K*0.25
C *****
GO TO 60
40 IF(N(J+1,K).EQ.0) GO TO 100
IF(K.EQ.1) GO TO 50
IF(N(J,K-1).NE.0.OR.N(J+1,K-1).NE.0) GO TO 100
C *****
C CASE 3 -- GRID SQUARES J,K AND J+1,K ARE NON-EMPTY, BUT
C J,K-1 AND J+1,K-1 ARE EMPTY. IN THIS CASE THE
C ASSIGNED POSITION IS THE POINT MIDWAY BETWEEN
C THE CENTERS OF THE TWO NON-EMPTY SQUARES.
C *****

```

```

50 SD=D(J,K)*N(J,K)+D(J+1,K)*N(J+1,K)
   SN=N(J,K)+N(J+1,K)
   TLONG=92.-J*0.25
   TLAT=-4.+K*0.25-0.125
C                                     *****
C 60 FILED=SD/SN
   LONG=TLONG
   DMLONG=(TLONG-LONG)*60.
   LAT=TLAT
   DMLAT=(TLAT-LAT)*60.
   WRITE(2,1000) LAT,DMLAT,LONG,DMLONG,FILED
C *****
C CASE 4 -- DATA FITS NONE OF THE ABOVE THREE CASES. IN
C           THIS CASE THE FILTERED VALUE IS NOT COMPUTED.
C *****
100 CONTINUE
   RETURN
   END

```

```

PROGRAM FILTGRID
C *****
C INPUTS BINARY N AND D ARRAYS AND THEN CALLS SUBROUTINE
C FILTDATA TO COMPUTE FILTERED BATHYMETRY OR FILTERED
C FREE-AIR GRAVITY ANOMALY.
C *****
COMMON N(64,56),D(64,56)
BUFFER IN (1,1) (N,N(64,56))
BUFFER IN (1,1) (D,D(64,56))
CALL FILTDATA
REWIND 1
END

```

```

PROGRAM FILTHICK
*****
C  COMPUTES THICKNESS OF CRUSTAL LAYERS, TOTAL THICKNESS OF
C  CRUST, AND DEPTH TO MANTLE FOR GRIDDED DATA.  FORMS N
C  ARRAY OF THE NUMBER OF FREE-AIR GRAVITY ANOMALY VALUES
C  IN EACH GRID SQUARE AND D ARRAY OF THE CORRESPONDING
C  COMPUTED DEPTH TO MANTLE.  CALLS SUBROUTINE FILTDATA TO
C  COMPUTE FILTERED DEPTH TO MANTLE.
C  *****
COMMON N(64,56),D(64,56)
1000 FORMAT (2I10,I4,F8.0,4X,F8.0,F7.0)
1001 FORMAT (2I10,I4,F8.0,6F8.0)
*****
C  INPUT PARAMETERS FOR COMPUTATION OF LAYER THICKNESS AND
C  DEPTH TO MANTLE ARE SET BY THE FOLLOWING 10 STATEMENTS.
C  *****
R1=1.03
R2=2.0
R3=2.6
R4=2.9
R5=3.28
DR53=R5-R3
DR54=R5-R4
A=10354.5417
B=2.385058341
RT3=R3*1100.

C  *****
10 READ(1,1000) IX,IY,NG,G,T1,T2
C  *****
C  COMPUTATION OF LAYER THICKNESS AND DEPTH TO MANTLE IS
C  EFFECTED BY THE FOLLOWING 19 STATEMENTS.
C  *****
IF(EOF(1)) GO TO 100
SRT2=R1*T1+R2*T2
ST2=T1+T2
TM2=A-B*G+SRT2
TEST=TM2-R5*ST2
IF(TEST.LT.0) GO TO 10
ST3=ST2+1100.
TM3=TM2+RT3
TEST=TM3-R5*ST3
IF(TEST.GT.0) GO TO 20
T=(TM2-R3*ST2)/DR53
CT=T-T1
T4=0
T3=T-ST2
GO TO 30
20 T=(TM3-R4*ST3)/DR54
CT=T-T1
T4=T-ST3
T3=1100.

C  *****
30 WRITE(10,1001) IX,IY,NG,G,T1,T2,T3,T4,CT,T
D(IX,IY)=T
N(IX,IY)=NG
GO TO 10
100 CALL FILTDATA
END

```

```

PROGRAM GRIDDATA
*****
C DIVIDES RECTANGULAR AREA INTO GRID SQUARES AND ASSIGNS
C TO EACH OF THESE SQUARES TWO INDICES COMPUTED FROM
C LONGITUDE AND LATITUDE, DESIGNATED J AND K, AND NUMBERED
C CONSECUTIVELY FROM THE SW CORNER OF THE GRID. SCANS
C INPUT FILE AND COMPUTES TWO ARRAYS: N(J,K), AN INTEGER
C ARRAY OF THE NUMBER OF DATA VALUES, AND D(J,K), A REAL
C ARRAY OF THE AVERAGE DATA VALUE IN EACH GRID SQUARE.
C COMPUTES THE AVERAGE, STANDARD DEVIATION, MINIMUM, AND
C MAXIMUM OF THE INPUT DATA VALUES.
C *****
C DIMENSION IDATA(15,100),IHDR(20),NUATA(64,56),DATA(64,56)
106 FORMAT(10NGDOBIN HEADER RECORD IS:1/X,20A4)
110 FORMAT(1H0,22I6)
111 FORMAT(1H ,22F6.0)
112 FORMAT(1 MEAN VALUE = 1,F6.0)
113 FORMAT(1 STANDARD DEVIATION = 1,F6.1)
114 FORMAT(1 MINIMUM VALUE = 1,F6.0)
115 FORMAT(1 MAXIMUM VALUE = 1,F6.0)
116 FORMAT(1H1)
117 FORMAT(1 NUMBER OF VALUES = 1,F6.0)
C *****
C THE FOLLOWING 5 STATEMENTS ARE THE INPUT PARAMETERS FOR
C A 15X GRID CONSTRUCTED IN THE AREA FROM 76W TO 92W AND
C FROM 4S TO 10N.
C *****
C OLAT=-40000
C OLON=-920000
C ULAT=100000
C ULON=-760000
C DEL=2500
C *****
C OMIN=100000
C OMAX=-100000
10 BUFFER IN (1,0) (IHDR,IHDR(20))
IF(EOF(1)) GO TO 50
WRITE(61,106) (IHDR(I),I=1,16)
20 BUFFER IN (1,1) (IDATA,IDATA(15,100))
IF(EOF(1)) GO TO 10
II=LENGTHF(1)/15
DO 30 I=1,II
PLAT=IDATA(4,I)
PLON=IDATA(5,I)
PVAL=IDATA(10,I)
C *****
C NOTICE THAT THE QUANTITY ASSIGNED BY THE ABOVE STATEMENT
C TO THE VARIABLE PVAL IS DETERMINED BY THE FOLLOWING
C CONVENTION:
C IDATA(10,I)=DEPTH
C IDATA(13,I)=MAGNETIC ANOMALY
C IDATA(14,I)=FREE-AIR GRAVITY ANOMALY
C *****
IF(PVAL.EQ.100000) GO TO 30
IF(PLAT.LT.OLAT.OR.PLAT.GE.ULAT) GO TO 30
IF(PLON.LT.OLON.OR.PLON.GE.ULON) GO TO 30

```

```

IX=(PLON-OLON)/DEL+1
IY=(PLAT-OLAT)/DEL+1
OATA(IX,IY)=OATA(IX,IY)+PVAL
NDATA(IX,IY)=NDATA(IX,IY)+1
TDATA=TDATA+PVAL
TSDATA=TSDATA+PVAL**2
SDATA=SDATA+1
IF(PVAL.GT.DMAX) DMAX=PVAL
IF(PVAL.LT.DMIN) DMIN=PVAL
30 CONTINUE
GO TO 20
50 DO 60 J=1,64
DO 60 K=1,56
60 OATA(J,K)=OATA(J,K)/NDATA(J,K)
BUFFER OUT (2,1) (NDATA,NDATA(64,56))
BUFFER OUT (2,1) (OATA,OATA(64,56))
ENDFILE 2
WRITE(10,116)
DO 61 K=1,56
WRITE(10,110) (NDATA(J,K),J=1,22)
61 WRITE(10,111) (OATA(J,K),J=1,22)
WRITE(10,116)
DO 62 K=1,56
WRITE(10,110) (NDATA(J,K),J=23,44)
62 WRITE(10,111) (OATA(J,K),J=23,44)
WRITE(10,116)
DO 63 K=1,56
WRITE(10,110) (NDATA(J,K),J=45,64)
63 WRITE(10,111) (OATA(J,K),J=45,64)
WRITE(10,116)
AV=TDATA/SDATA
SDEV=((SDATA*TSDATA-TDATA**2)/(SDATA*(SDATA-1)))**0.5
WRITE(10,112) AV
WRITE(10,113) SDEV
WRITE(10,114) DMIN
WRITE(10,115) DMAX
WRITE(10,117) SDATA
END

```



```

PROGRAM LISTGRID
C *****
C REFORMATS GRIDDED DATA FROM BINARY ARRAYS TO A BCD
C CARD IMAGE FILE.
C *****
  DIMENSION NG(64,56),G(64,56),NO(64,56),D(64,56)
1000 FORMAT(2I10,I4,F8.0,4X,F8.0)
  BUFFER IN (1,1) (NG,NO(64,56))
  BUFFER IN (1,1) (G,G(64,56))
  CALL SEFF(1)
  CALL SEFF(1)
  BUFFER IN (1,1) (NO,NO(64,56))
  BUFFER IN (1,1) (D,D(64,56))
  REWIND 1
  DO 10 K=1,56
  DO 10 J=1,64
    IF(NO(J,K).EQ.0.OR.NO(J,K).EQ.0) GO TO 10
    WRITE(2,1000) J,K,NG(J,K),G(J,K),D(J,K)
10 CONTINUE
  END

```

```

      PROGRAM THICKOMP
      *****
C     COMPUTES THICKNESS OF CRUSTAL LAYERS, TOTAL THICKNESS
C     OF CRUST, AND DEPTH TO MANTLE FOR PENDULUM STATION DATA.
C     *****
1000  FORMAT(2(I5,F5.1),2(6X,F6.0),3X,F4.0)
1001  FORMAT(2(I5,F5.1),6X,F6.0,6F8.0)
1002  FORMAT(2(I5,F5.1),F8.0)
C     *****
C     INPUT PARAMETERS FOR COMPUTATION OF LAYER THICKNESS AND
C     DEPTH TO MANTLE ARE SET BY THE FOLLOWING 10 STATEMENTS.
C     *****
      R1=1.03
      R2=2.0
      R3=2.6
      R4=2.9
      R5=3.28
      DR53=R5-R3
      DR54=R5-R4
      A=10354.5417
      B=2.3850583+1
      RT3=R3*1100.
C     *****
10  READ(1,1000) LAT,DMLAT, LONG,DMLONG,G,T1,T2
C     *****
C     COMPUTATION OF LAYER THICKNESS AND DEPTH TO MANTLE IS
C     EFFECTED BY THE FOLLOWING 19 STATEMENTS.
C     *****
      IF(EOF(1)) GO TO 100
      SRT2=R1*T1+R2*T2
      ST2=T1+T2
      TM2=A-B*G+SRT2
      TEST=TM2-R5*ST2
      IF(TEST.LT.0) GO TO 10
      ST3=ST2+1100.
      TM3=TM2+RT3
      TEST=TM3-R5*ST3
      IF(TEST.GT.0) GO TO 20
      T=(TM2-R3*ST2)/DR53
      CT=T-T1
      T4=0
      T3=T-ST2
      GO TO 30
20  T=(TM3-R4*ST3)/DR54
      CT=T-T1
      T4=T-ST3
      T3=1100.
C     *****
30  WRITE(10,1001) LAT,DMLAT, LONG,DMLONG,G,T1,T2,T3,T4,CT,T
      WRITE(2,1002) LAT,DMLAT, LONG,DMLONG,T
      GO TO 10
100  END

```

## APPENDIX II

GENERAL DISCUSSION AND DERIVATION OF A  
50-KM STANDARD SECTION

The observed free-air gravity anomaly  $G$  is related to the gravitational attraction of a crustal model  $AC$  by the following equation:  $G=AC-AT$ , where  $AT$  is the attraction of a theoretical model occupying the same space as the computed crustal model and above which the free-air anomaly is zero. If there are no lateral inhomogeneities below the base of the model, then isostatic equilibrium prevails at this depth. Consequently, the theoretical model is called a standard section.

Table 2 presents some of the more common standard sections found in the geophysical literature.

From a comparison of 6 sea stations and 7 land stations at which there were both seismic and gravity data, Worzel and Shurbet (1955) derived standard sections for oceanic and continental crusts. By constraining these two sections to be in isostatic equilibrium (in the sense of equal mass per unit area) at the base of the continental crust (33 km), they computed a mantle density of  $3.27 \text{ g/cm}^3$ . Notice that the tabulated  $0.085 \times 10^5 \text{ -g/cm}^2$  discrepancy in the computed mass per unit area at 33 km between the oceanic and continental sections is insignificant relative to a  $0.01\text{-g/cm}^3$  change in mantle density.

Table 2. Standard section comparison.

Source		Worzel & Shurbet (1955) A	Worzel & Shurbet (1955) B	Talwani, et al. (1959b)	Worzel (1965) A	Worzel (1965) B	Couch (1969)	Computed
Water	T	5.00			4.90		3.70	4.05
Layer	D	1.03			1.03		1.03	1.03
Sediment	T	1.00			0.70		0.50	0.46
Layer	D	2.30			2.30		2.15	2.00
Transition	T				1.70		0.80	1.10
Layer	D				2.55		2.74	2.60
Oceanic	T	4.50	33.00	32.00	4.20	33.00	5.00	4.00
Layer <sup>a</sup>	D	2.84	2.84	2.87	2.90	2.90	3.00	2.90
Mantle	T*	10.50	33.00	32.00	11.50	33.00	10.00	9.61
Layer	D	3.27	3.27	3.40	3.40	3.40	3.30	3.32
Mass per unit area at a depth of								
20 km		51.30	56.80	57.40	52.07	58.00	55.08	54.05
30 km		84.00	85.20	86.10	86.07	87.00	88.08	87.25
32 km		90.54	90.88	91.84	92.87	92.80	94.68	93.89
33 km		93.80	93.72	95.24	96.27	95.70	97.98	97.21
40 km		116.70	116.61	119.04	120.07	119.50	121.08	120.45
50 km		149.40	149.31	153.04	154.07	153.50	154.08	153.65

T = thickness in km

T\* = depth to Moho in km

D = density in g/cm<sup>3</sup><sup>a</sup>oceanic layer also designates crustal layer when only one layer is given

The standard section of Talwani et al. (1959b) is based on seismic refraction data in the area of the Puerto Rico Trench. The depth of this section is 32 km, in order to clear the root beneath Puerto Rico.

Worzel (1965) averaged all available seismic refraction data to get a marine crustal section and mean mantle density of  $3.40 \text{ g/cm}^3$ . Although he stated that this column is in isostatic balance with a sea-level column 33 km thick and with a mean density of  $2.90 \text{ g/cm}^3$ , a  $0.572 \times 10^5 \text{ g/cm}^2$ -discrepancy in the mass per unit area at 33 km between the respective mass columns indicates that the sea-level continental column must have a mean density of 2.92 rather than 2.90.

The standard section presented by Couch (1969) is constrained to be in isostatic balance at 50 km with the oceanic section of Worzel (1965).

The historical basis for the use of standard sections in the construction of crustal models begins with the assumption that lateral density changes do not occur below a relatively shallow depth. Referred to hereafter as the homogeneous mantle hypothesis, this assumption is based primarily on early isostatic computations (Vening Meinesz, 1948) and observations of earthquake seismology.

At first, it was thought that lateral inhomogenities existed only in the crust, implying that even the upper mantle is laterally homogeneous. In fact, with one exception, all the crustal sections

presented by Worzel (1965) are constructed based on this premise. An increasing body of marine seismic refraction data (Raitt, 1956; Ewing and Ewing, 1959; LePichon et al., 1965), however, confirmed the existence of low-velocity mantle arrivals under ridge crests and forced geophysicists to admit lateral variations of upper mantle density in their crustal sections. For example, using the standard section of Talwani et al. (1959b) extended to a depth of 40 km, Talwani et al. (1965) constructed 3 crustal sections of the Mid Atlantic Ridge, each showing a prism of low-density upper mantle material, penetrating to a depth of less than 40 km immediately beneath the ridge crest and extending laterally 1000 km from the ridge axis below a thickening wedge of normal mantle.

As a consequence of the homogeneous mantle hypothesis, it is obviously essential (Talwani, 1964) that all standard sections chosen everywhere have the same total mass to a fixed depth. The fact that the standard sections compared in Table 2 do not agree in this respect unless constrained to do so at any of the common depths for terminating crustal models casts doubts on the validity of this hypothesis, at least in reference to depths as shallow as those for which it has been applied.

Other evidence which contradict the hypothesis are: petrologic models such as those discussed by Forsyth and Press (1971)

demonstrating lateral variations in density throughout a 70- to 100-km-thick lithosphere, studies of the petrological-physical properties of the upper mantle (Clark and Ringwood, 1964) resulting in the conclusion that isostatic compensation is not complete until 400 km, comparison of recent seismic models (Green and Hales, 1968; Archambeau et al., 1969; Johnson, 1967; Lewis and Meyer, 1968; and Anderson, 1967) implying lateral differences of P velocity extending possibly to depths of 400 km and more, and isostatic calculations for the U. S. made by Lewis and Dorman (1970) indicating that lateral density changes take place to a depth of at least 400 km--a rough limit imposed by the long-wavelength resolution of the data.

In light of the quality and diversification of the above evidence, it must be concluded that the homogeneous mantle hypothesis be discarded, and the basic premise of standard section equivalence expressed by Talwani (1964) be amended to take into account deep-seated lateral changes in density. One way to account for these changes is to replace standard sections by a theoretical crustal model whose structure varies with geographic position or crustal age, as suggested by the two-dimensionality of petrologic models and the success of an empirical relationship between age and depth (Sclater et al., 1971). However, until a suitable theoretical model is adopted, standard sections remain a necessity in crustal modeling. Therefore, standard sections themselves must be functions of position or age,

and lateral changes in density beneath computed crustal models must be taken into account or assumed insignificant.

Examples of arguments supporting the assumption of insignificant lateral changes in density at depth are as follows: 1) Talwani et al. (1965) ruled out significant lateral changes in density below 40 km based on steep gradients in the bouguer anomaly. 2) Couch (1969) argued for the lack of significant lateral changes in density below 50 km based on the wavelength of the observed anomalies and extra-gravimetric evidence.

For the Panama Basin, it is tempting to use the standard section of Worzel (1965), because it is based on all available seismic refraction data from several ocean basins and is, therefore, closer to a world average section than any of the other sections which have been used. However, as discussed above, it is felt that a better section could be derived based on an average of all seismic refraction data in a patch of normal oceanic crust as near as possible both in space and in time to the study area. Of course, the best possible patch of crust for this purpose is the Panama Basin itself. Unfortunately, however, the absence of seismic refraction data rules out this choice.

As indicated by marine seismic refraction data, the oceanic mantle appears, to a first approximation at least, to be made up of an anomalous zone of low density upper mantle within 250 km of



active spreading centers and a roughly constant normal mantle elsewhere. Furthermore, according to published petrologic models, the most rapid changes in mantle density also occur in this area. Therefore, seismic refraction stations within 250 km of active ridges should not be used for the determination of standard sections.

The above conclusion rules out the next obvious choice for a crustal patch, namely, an area roughly the same age as the Panama Basin, because a statistically significant number of seismic refraction stations have not been located in that small region of oceanic crust younger than 10 m. y. but farther than 250 km from active spreading centers.

The third and final choice for a crustal patch is an area near the Panama Basin, but in older oceanic crust. The area chosen for this purpose is depicted in Figure 17 along with the seismic refraction stations located therein. This particular area is selected due to its lack of geologic complexity, its relatively high density of seismic refraction data, and its proximity to the Panama Basin. Although its northern and southern boundaries are completely arbitrary, its eastern boundary is chosen at anomaly 4 (17 m. y.) to exclude all those stations in the zone of anomalous mantle while including the youngest stations possible in normal crust, and its western boundary is chosen at anomaly 17 (43 m. y.) to include a significant number of

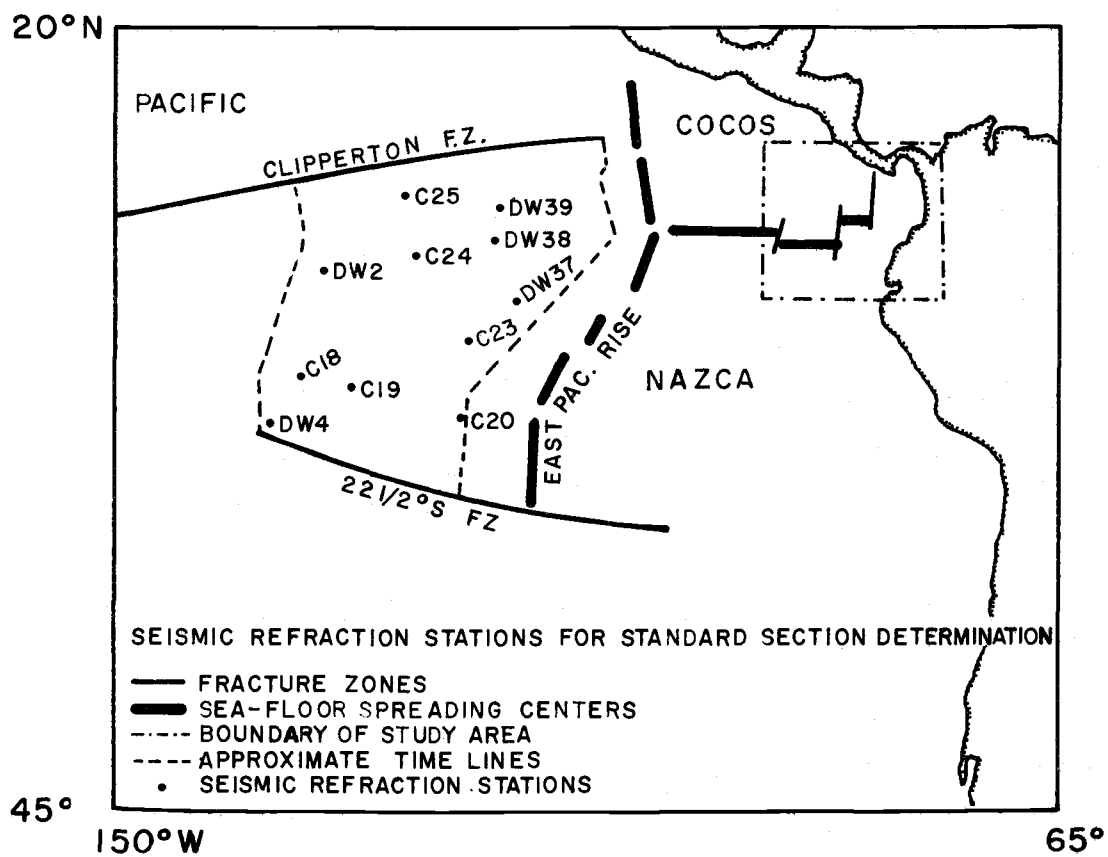


Figure 17. Location map for seismic refraction stations used for standard section determination.

seismic stations while corresponding to an age which makes the average age of the crustal patch 25 m. y.

Table 3 presents the tabulated and averaged mass columns derived from the eleven seismic refraction stations shown in Figure 17. Velocities were converted to densities with the Ludwig, Nafe, and Drake (1970) curves. Notice that for no apparent geologic reason, the mantle velocity and, hence, the computed attraction of the mass column for station DW4 is significantly greater than that of the other stations (Figure 18). Therefore, this station is rejected, and a new average mass column is computed and tabulated based on the 10 remaining stations. It might also be argued, based on the geologic hypothesis of a preexisting spreading center (Herron, 1972) on or near which stations DW38 and DW39 lie, that these stations should also be omitted from the final average because they might not represent normal mantle. However, both their mantle velocity and attraction fall well within the range determined by the other stations. Hence, they are preserved while station DW4 is discarded.

The standard section is derived on the basis of the following three criterion, listed in order of priority: 1) The attraction of the standard section must be as close as possible to 6442.1, the average attraction of the 10 seismically derived sections. Notice that due to roundoff errors there is a 5.3-mgal difference between this number

Table 3. Computation of 50-km standard section.

Station		C18	C19	C20	C23	C24	C25	DW2	DW4	DW37	DW38	DW39	(1)	(2)	(3)
Water Layer	T	4.19	4.07	3.58	4.33	4.46	4.26	4.50	4.49	4.35	3.82	4.14	4.20	4.17	4.05
	V	1.500	1.499	1.496	1.500	1.501	1.499	1.502	1.502	1.501	1.498	1.499			
	D	1.03	1.03	1.03	1.03	1.03	1.03	1.03	1.03	1.03	1.03	1.03	1.03	1.03	1.03
Sediment Layer	T	0.20	0.22	0.27	0.34	0.38	0.53	0.51	0.39	0.19	0.55	0.37	0.36	0.36	0.46
	V	2.15	2.15	2.15	2.15	2.15	2.15	2.15	2.15	2.15	2.15	2.15			
	D	1.98	1.98	1.98	1.98	1.98	1.98	1.98	1.98	1.98	1.98	1.98	1.98	1.98	2.0
Transition Layer	T	1.59	0.81	0.73	1.20	1.18	0.66	1.42	0.70	1.23	1.14	0.97	1.06	1.09	1.10
	V	5.04	5.22	5.09	6.02	4.92	5.78	5.75	5.91	5.62	4.75	4.88			
	D	2.53	2.57	2.54	2.70	2.52	2.66	2.65	2.68	2.63	2.44	2.51	2.58	2.58	2.6
Oceanic Layer	T	4.57	4.60	4.24	3.31	4.03	4.19	5.31	5.52	2.54	3.38	3.86	4.14	4.00	4.00
	V	6.91	6.69	6.48	6.90	6.84	6.90	7.05	6.91	7.10	7.07	6.91			
	D	2.92	2.85	2.81	2.92	2.89	2.92	2.96	2.92	2.98	2.97	2.92	2.91	2.91	2.9
Mantle Layer	T	10.55	9.70	8.82	9.18	10.05	9.64	11.74	11.10	8.31	8.89	9.34	9.76	9.62	9.61
	V	8.14	8.00	8.12	8.30	8.21	8.16	8.28	8.88	8.38	8.31	8.06			
	D	3.31	3.24	3.29	3.36	3.33	3.32	3.35	3.58	3.40	3.37	3.26	3.35	3.32	3.32
Attraction		6400.61	6305.56	6434.76	6506.90	6414.94	6432.66	6427.36	6819.68	6599.70	6556.84	6341.74	6476.4	6442.1	6442.0
													(6483.1)	(6436.8)	

T = thickness in km

V = velocity of sound in km/sec

D = density in g/cm<sup>3</sup>

Attraction = gravitational attraction in milligals of 50-km section, computed with infinite-slab approximation

(1) Section computed by averaging all 11 seismic refraction stations. Tabulated attraction is the average of the 11 stations; parenthetical attraction is the attraction of the average section.

(2) Section computed by all but station DW4.

(3) Standard section obtained by adjusting section (2) so that its attraction is nearly equal to the tabulated average.

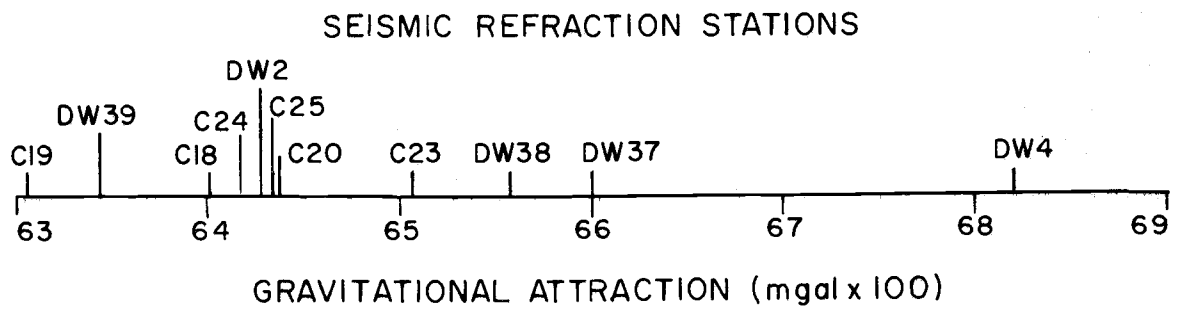


Figure 18. Distribution of the gravitational attraction of the 50-km sections determined for each of the seismic refraction stations.

and the attraction of the average section. 2) With the exception of the mantle and water layers the densities are rounded off to the nearest tenth. 3) The thickness of the various layers should be close to those of the average section, but remain as simple as possible. This criterion was used to justify the 0.1-mgal difference between the attractions of the standard and averaged sections. The resulting section is shown both in tables 2 and 3.